TU Delft

Delft University of Technology

A high-order 2D-plate macro-element model for the analysis of bonded joints

Calì, Marcello; Schwartz, Sébastien; Lachaud, Frédéric; De Freitas, Sofia Teixeira; Paroissien, Éric

DOI
10.1016/j.ijsolstr.2025.113787

Publication date
2026

Document Version
Final published version

Published in
International Journal of Solids and Structures

Citation (APA)
Calì, M., Schwartz, S., Lachaud, F., De Freitas, S. T., & Paroissien, É. (2026). A high-order 2D-plate macro-element model for the analysis of bonded joints. *International Journal of Solids and Structures*, *327*, Article 113787. https://doi.org/10.1016/j.ijsolstr.2025.113787

Important note
To cite this publication, please use the final published version (if applicable).
Please check the document version above.

Copyright
Other than for strictly personal use, it is not permitted to download, forward or distribute the text or part of it, without the consent of the author(s) and/or copyright holder(s), unless the work is under an open content license such as Creative Commons.

Takedown policy
Please contact us and provide details if you believe this document breaches copyrights.
We will remove access to the work immediately and investigate your claim.

This work is downloaded from Delft University of Technology.
For technical reasons the number of authors shown on this cover page is limited to a maximum of 10.

Green Open Access added to TU Delft Institutional Repository
as part of the Taverne amendment.

More information about this copyright law amendment
can be found at https://www.openaccess.nl.

Otherwise as indicated in the copyright section:
the publisher is the copyright holder of this work and the
author uses the Dutch legislation to make this work public.

International Journal of Solids and Structures 327 (2026) 113787

Contents lists available at ScienceDirect

International Journal of Solids and Structures

journal homepage: www.elsevier.com/locate/ijsolstr

A high-order 2D-plate macro-element model for the analysis of bonded joints

Marcello Calì [a], Sébastien Schwartz [a,*], Frédéric Lachaud [a], Sofia Teixeira De Freitas [b,c], Éric Paroissien [a]

[a] Institut Clément Ader, Université de Toulouse, ISAE-SUPAERO, INSA, IMT MINES ALBI, UTIII, CNRS, 3 Rue Caroline Aigle, Toulouse, 31400, France
[b] Aerospace Engineering, TU Delft, Delft, The Netherlands
[c] IDMEC, Instituto Superior Técnico, Lisbon, Portugal

ARTICLE INFO

Keywords:
Macro-element
Higher order displacement field
Single-lap joint
Simplified stress analysis
Advanced plate theory

ABSTRACT

Adhesive bonding has emerged as an attractive solution for the joining of lightweight structures, yet accurate stress analysis remains computationally demanding when relying on Finite Elements (FE). This paper introduces a novel plate Macro-Element (ME) formulation that extends previous beam-type approaches to enable three-dimensional stress analysis of bonded joints. High-order polynomial expansions are employed to describe the displacement field of the adherends, while the adhesive is modeled as an elastic foundation. Governing equations are derived using a variational principle and integrated within a standard FE framework. Through the derivation of a special stiffness matrix, a ME can simulate an entire overlap with just one element. The proposed methodology is validated against FE results for a single-lap bonded joint with a thin adhesive layer. The influence of different higher-order displacement assumptions and constitutive models is investigated. The results show that their inclusion in the formulation improves the solution accuracy.

1. Introduction

Adhesive bonding is recognized as one of the most appealing solutions for joining of lightweight structures thanks to its elevate strength-to-weight ratio. For this reason, it has recently experienced swift development in a number of high-tech industries such as aerospace and automotive, but also electronics and medical surgery (Ebnesajjad, 2009; Pizzi and Mittal, 2003). The design of a joint relies on the existence of computational tools that allow to estimate the stress state of the assembly during its operational life, reducing the need for expensive experiments. However, very accurate analyses based on Finite Elements (FE) usually require considerable computational time, limiting the feasibility of structural optimization. As a result, approximated methods capable of operating in reduced time are essential and have become a key focus of research.

Over the last two decades, multiple reviews (da Silva et al., 2009; Da Silva et al., 2009; Banea and Silva, 2009; He, 2011; Budhe et al., 2017; Tserpes et al., 2022; Wei et al., 2024) have collected the advancements on the topic, covering the analytical, semi-analytical and numerical approaches to the stress analysis of bonded joints. Among the various joint configurations, the Single Lap Joint (SLJ) emerges as the classic example case of study, and is therefore commonly adopted by the authors as a benchmark for the techniques presented below.

Analytical models are based on the laws of conservation and, given the appropriate simplifying assumptions, yield solutions in the form of ready-to-use formulas. Fundamental work was done by Volkersen (1938) in 1938 applying the concept of differential shear to the load transfer in mechanical assemblies. In his model, the adherends of a SLJ were treated as deformable bars and the adhesive as an infinite series of shear springs. This kind of formulation is often referred to as "beams on elastic foundation" model. The structure was considered in its entirety and with simple supports at the boundaries, allowing for the determination of the internal loads. Successive studies progressively refined Volkersen's model, each building upon the previous with incremental improvements. Goland and Reissner (1944) included bending moment and peel stress in the analysis treating the adherends as deformable beams and defining a bending moment factor dependent on geometry and normal load. Hart-Smith (1973) accounted for the geometric effect of the adhesive thickness in the moment balance and for its flexibility in shear, and thus gave a modified expression for the bending moment factor. Additional advancements considered increasingly complex displacement fields for the adhesive layer, as seen in Ojalvo and Eidinoff (1978), as well as more sophisticated kinematics for the adherends, such as in the work by Oplinger (1991) and Luo and Tong (2007). Nonetheless, the applicability of such models is highly restricted by the boundary condition assumption of simple support

* Corresponding author.
E-mail address: Sebastien.SCHWARTZ@isae-supaero.fr (S. Schwartz).
URL: https://github.com/sschwart/research (S. Schwartz).

https://doi.org/10.1016/j.ijsolstr.2025.113787
Received 5 September 2025; Received in revised form 19 November 2025; Accepted 22 November 2025
0020-7683/© 2025 Elsevier Ltd. All rights are reserved, including those for text and data mining, AI training, and similar technologies.

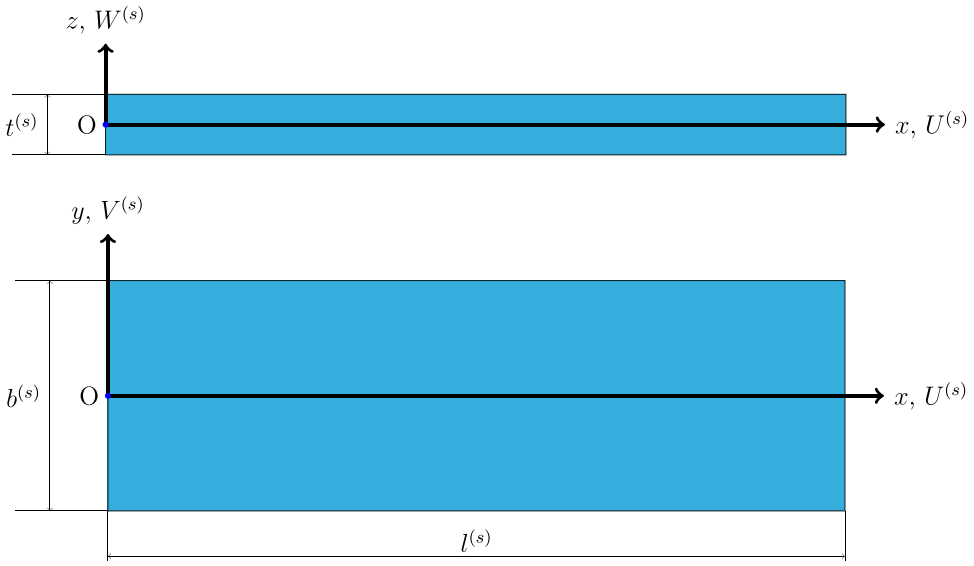

Fig. 1. Reference system for isolated plate.

and becomes greatly complicated, if not unfeasible analytically, when considering non-identical adherends. To overcome these limitations, alternative formulations focus solely on the overlap of the SLJ, often referred to as "sandwich", while assuming known conditions at its extremities. Early investigations were carried out by Williams (1975), who considered different substrates and proposed a mathematical form of the analytical solution accounting for the coupling between normal and shear stresses. An exact solution for this problem was later provided by Bigwood and Crocombe (1989), although neglecting the coupling between normal and shear stresses. Subsequent studies, including that of Frostig et al. (1999), implemented high-order displacement theories. Such additional complications, however, mean that a closed-form solution is only obtained in very simple cases. These models, which lead to a mathematical formulation but require computational support to produce an output, are then known as semi-analytical. More elaborate versions of them were given by Adams and Mallick (1992), Mortensen and Thomsen (2002) and Nguyen and Le Grognec (2021). Nonetheless, very few studies (Adams and Peppiatt, 1973; Oterkus et al., 2004) have incorporated three-dimensional effects such as finite width into simplified modeling frameworks.

The Macro-Element (ME) modeling belongs to the latter category of semi-analytical models. First introduced in 2007, it consists in a simplified analysis inspired by FE but requiring a very low computational burden compared to them. The method is based on the discretization of the structure into elements with special stiffness characteristics, whose interpolation function is not assumed but derived from the constitutive and equilibrium equations. Thanks to its specially formulated stiffness matrix, a ME can simulate an entire overlap with just one element. This key feature allows to overcome many of the challenges faced by previous models, including non-identical adherends, variable boundary conditions, and the need for refined meshing. In earlier formulations (Paroissien et al., 2007) the stiffness matrix was derived analytically, and its development followed an incremental path analogous to the one discussed earlier for analytical models. Numerous studies have validated the accuracy of such simplified ME analyses, proving good agreement with FE across different geometries (Paroissien et al., 2019). The method has also been successfully applied to model damage initiation and propagation in Double Cantilever Beam (DCB) tests (Lachaud et al., 2020), SLJ (Lelias et al., 2015), stepped joints (Orsatelli et al., 2024), and interface adhesive failure (Birro et al., 2020). In the later publication by Schwartz et al. (2024a), the procedure to derive the stiffness matrix is automated and generalized with a variational principle based on virtual work. This new approach allows for easy model enrichment, as demonstrated in Schwartz et al. (2024b). However, previous work has been restricted to beam-type kinematics and plane strain or stress hypotheses, limiting its applicability to more complex structures such as plates and shells.

In this paper, a new plate formulation based on a variational principle is presented. High-order displacement functions are used to define a solid ME to represent the adherends, while the adhesive is modeled as an elastic foundation. The method is validated against an equivalent FE model for the stress analysis of a SLJ. The influence of different higher-order displacement assumptions and constitutive models on solution accuracy is systematically investigated.

2. Methodology and formulation framework

2.1. Outline

Thanks to its specially formulated stiffness matrix, a ME can simulate an entire overlap with just one element.

The methodology to derive the ME is presented as follows. First, the fundamental underlying hypotheses are outlined along with their implications. Next, the governing equilibrium equations are derived using the virtual work principle. Finally, the stiffness matrix is written and its implementation within a solving algorithm is illustrated.

2.2. Hypotheses

The formulation is developed under the assumptions of linear elastic behavior for isotropic materials, static loading, and small displacements. The reference system used is illustrated in Fig. 1 for the isolated adherend plate and in Fig. 2 for the SLJ assembly.

In these hypotheses, let $U^{(s)}, V^{(s)}$ and $W^{(s)}$ represent the displacement functions of the sth substrate in the x, y and z directions, respectively. Using a series expansion, the general displacement of a point in

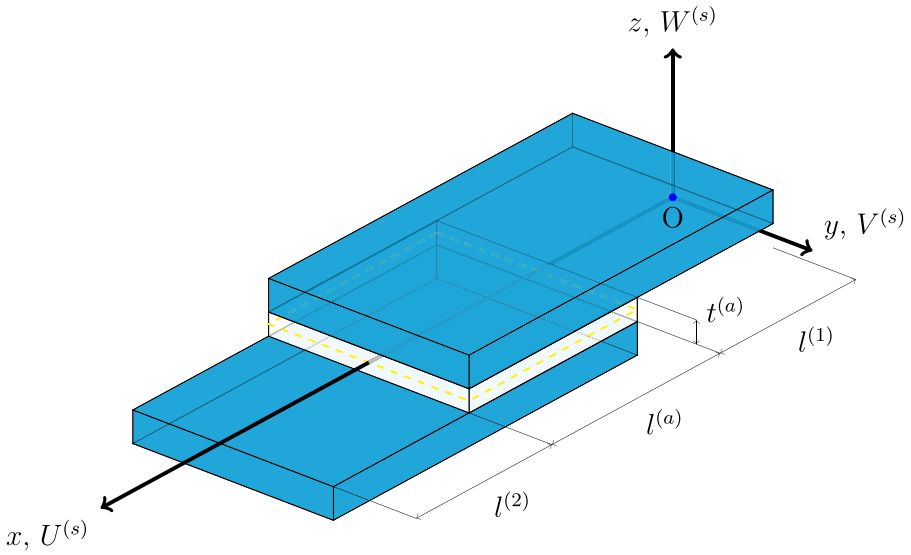

Fig. 2. Reference system for SLJ assembly.

the sth plate can be written as:

$$\begin{aligned} U^{(s)}(x,y,z) &= \sum_{j=0}^{n_y^{(s)}} \sum_{k=0}^{n_z^{(s)}} u_{jk}^{(s)}(x) \cdot y^j z^k \\ V^{(s)}(x,y,z) &= \sum_{j=0}^{m_y^{(s)}} \sum_{k=0}^{m_z^{(s)}} v_{jk}^{(s)}(x) \cdot y^j z^k \\ W^{(s)}(x,y,z) &= \sum_{j=0}^{p_y^{(s)}} w_j^{(s)}(x) \cdot y^j \end{aligned} \tag{1}$$

where $u_{jk}^{(s)}$ and $v_{jk}^{(s)}$ are the (j,k)th order displacement functions of the sth adherend plate and $n_y^{(s)}, n_z^{(s)}$ and $m_y^{(s)}, m_z^{(s)}$ the higher orders in the expansions, respectively. In plate kinematics, it is assumed that the thickness of the plate is very small compared to its other dimensions, so that $W^{(s)}$ can be considered a function of only the in-plane coordinates x, y. Therefore, only the series expansion for the y direction is considered, where $w_j^{(s)}$ is the jth order displacement function and $p_y^{(s)}$ the higher order in the series. It should be emphasized that each term in the series, according to its order, directly corresponds to a specific displacement or deformation shape that the adherend is capable of exhibiting under loading. Higher-order terms enable the capture of increasingly complex deformations. Although this formulation does not directly lead to standard plate theories due to the series expansion in y, they can be still recovered introducing the additional assumption of cylindrical bending and disregarding the y-coordinate dependence. In this case, well-known plate theories can be attained by appropriately adjusting $(n_z^{(s)}, m_z^{(s)})$. For instance, if $(n_z^{(s)}, m_z^{(s)}) = (1,1)$ the Reissner–Mindlin theory with adherend shearing is obtained, while the Reddy theory presented in Reddy (1984) is retrieved with (3,3).

The strain–displacement relationships can be expressed in a compact form as:

$$\varepsilon_{qr}^{(s)} = \frac{1}{2}\left(\frac{\partial D_q^{(s)}}{\partial x_r} + \frac{\partial D_r^{(s)}}{\partial x_q}\right) \tag{2}$$

where $\varepsilon_{qr}^{(s)}$ represents the strain components of the sth adherend, $D_q^{(s)}$ and $D_r^{(s)}$ denote a generic displacement at a point of the sth adherend and the subscripts q and r indicate the directions associated with the spatial coordinates. The strain vector for the plate, obtained inserting Eq. (1) in Eq. (2), then takes the form:

$$\begin{aligned} \varepsilon_{xx}^{(s)} &= \sum_{j=0}^{n_y^{(s)}} \sum_{k=0}^{n_z^{(s)}} \frac{du_{jk}^{(s)}(x)}{dx} \cdot y^j z^k \\ \varepsilon_{yy}^{(s)} &= \sum_{j=1}^{m_y^{(s)}} \sum_{k=0}^{m_z^{(s)}} v_{jk}^{(s)}(x) \cdot j y^{j-1} z^k \\ \varepsilon_{zz}^{(s)} &= 0 \\ \varepsilon_{xy}^{(s)} &= \frac{1}{2}\left[\sum_{j=0}^{m_y^{(s)}} \sum_{k=0}^{m_z^{(s)}} \frac{dv_{jk}^{(s)}(x)}{dx} \cdot y^j z^k + \sum_{j=1}^{n_y^{(s)}} \sum_{k=0}^{n_z^{(s)}} u_{jk}^{(s)}(x) \cdot j y^{j-1} z^k\right] \\ \varepsilon_{xz}^{(s)} &= \frac{1}{2}\left[\sum_{j=0}^{p_y^{(s)}} \frac{dw_j^{(s)}(x)}{dx} \cdot y^j + \sum_{j=0}^{n_y^{(s)}} \sum_{k=1}^{n_z^{(s)}} u_{jk}^{(s)}(x) \cdot k y^j z^{k-1}\right] \\ \varepsilon_{yz}^{(s)} &= \frac{1}{2}\left[\sum_{j=1}^{p_y^{(s)}} w_j^{(s)}(x) \cdot j y^{j-1} + \sum_{j=0}^{m_y^{(s)}} \sum_{k=1}^{m_z^{(s)}} v_{jk}^{(s)}(x) \cdot k y^j z^{k-1}\right] \end{aligned} \tag{3}$$

It is worth mentioning that, for the sake of simplicity, the series can be kept starting from index zero, as the corresponding terms vanish automatically. This convention will be adopted in the following developments.

Based on Hooke's law, the stress–strain relations are given by:

$$\begin{aligned} \sigma_{qq}^{(s)} &= \frac{E^{(s)}}{\left(1+\nu^{(s)}\right)\left(1-2\nu^{(s)}\right)}\left[\left(1-\nu^{(s)}\right)\varepsilon_{qq}^{(s)} + \nu^{(s)}\left(\varepsilon_{rr}^{(s)} + \varepsilon_{hh}^{(s)}\right)\right] \\ \tau_{qr}^{(s)} &= 2G^{(s)}\varepsilon_{qr}^{(s)} \end{aligned} \tag{4}$$

where σ_{qq} and τ_{qr} are the normal and shear stresses relative to the directions specified by the subscripts q and r, E the Young Modulus, ν the Poisson coefficient and the shear modulus G can be assessed with the classic formula $G = E/(2(1+\nu))$. Eq. (4) can be rewritten in the

x, y, z reference system with a simpler matrix expression as:

$$\begin{Bmatrix} \sigma_{xx} \\ \sigma_{yy} \\ \sigma_{zz} \\ \tau_{xy} \\ \tau_{xz} \\ \tau_{yz} \end{Bmatrix}^{(s)} = \begin{bmatrix} E' & \nu' E' & \nu' E' & 0 & 0 & 0 \\ \nu' E' & E' & \nu' E' & 0 & 0 & 0 \\ \nu' E' & \nu' E' & E' & 0 & 0 & 0 \\ 0 & 0 & 0 & 2G' & 0 & 0 \\ 0 & 0 & 0 & 0 & 2G' & 0 \\ 0 & 0 & 0 & 0 & 0 & 2G' \end{bmatrix}^{(s)} \begin{Bmatrix} \varepsilon_{xx} \\ \varepsilon_{yy} \\ \varepsilon_{zz} \\ \varepsilon_{xy} \\ \varepsilon_{xz} \\ \varepsilon_{yz} \end{Bmatrix}^{(s)} \tag{5}$$

where the introduction of the E', ν' and G' notation allows to simply modify the constitutive relations and to account for various models or effects, such as the confinement of the adhesive between the adherends — which influences the effective material moduli (Anasiewicz and Kuczmaszewski, 2021, 2022) — or the assumptions of plane stress and plane strain. The use of effective moduli offers a practical means of incorporating them into the analysis.

Finally, the numerical internal moments of (j,k)th order relative to each stress component are defined as:

$$\begin{aligned} M^{(s)}_{xx,jk} &= \int_{S^{(s)}} y^j z^k \cdot \sigma^{(s)}_{xx}\, dS^{(s)} & M^{(s)}_{xy,jk} &= \int_{S^{(s)}} y^j z^k \cdot \tau^{(s)}_{xy}\, dS^{(s)} \\ M^{(s)}_{yy,jk} &= \int_{S^{(s)}} y^j z^k \cdot \sigma^{(s)}_{yy}\, dS^{(s)} & M^{(s)}_{xz,jk} &= \int_{S^{(s)}} y^j z^k \cdot \tau^{(s)}_{xz}\, dS^{(s)} \\ M^{(s)}_{zz,jk} &= \int_{S^{(s)}} y^j z^k \cdot \sigma^{(s)}_{zz}\, dS^{(s)} & M^{(s)}_{yz,jk} &= \int_{S^{(s)}} y^j z^k \cdot \tau^{(s)}_{yz}\, dS^{(s)} \end{aligned} \tag{6}$$

where $S^{(s)}$ is the cross-sectional area $dydz$ of the sth adherend, where the stress is applied. It is important to note that, by substituting Eq. (3) into Eq. (5) and subsequently Eq. (5) into Eq. (6), an expression of the internal loads in terms of the displacement functions can be obtained.

The adhesive layer is modeled as a foundation of linear elastic springs connecting the two plates. The force generated by the springs is proportional to the relative displacement between the overlapping adherends, and constant through the adhesive thickness $t^{(a)}$. The relative displacement of the springs extremities can be decomposed along the x, y, z directions, resulting in three corresponding strain components. Under the assumption of small displacement, their expressions are given by:

$$\begin{aligned} \varepsilon^{(a)}_{xz} &= \frac{U^{(a)}_{sup} - U^{(a)}_{inf}}{2t^{(a)}} \\ \varepsilon^{(a)}_{yz} &= \frac{V^{(a)}_{sup} - V^{(a)}_{inf}}{2t^{(a)}} \\ \varepsilon^{(a)}_{zz} &= \frac{W^{(a)}_{sup} - W^{(a)}_{inf}}{t^{(a)}} \end{aligned} \tag{7}$$

where the subscripts "*sup*" and "*inf*" denote the upper and lower spring extremities. To simplify the notation, the relative displacements are defined as:

$$\Delta U^{(a)} = U^{(a)}_{sup} - U^{(a)}_{inf}, \quad \Delta V^{(a)} = V^{(a)}_{sup} - V^{(a)}_{inf}, \quad \Delta W^{(a)} = W^{(a)}_{sup} - W^{(a)}_{inf} \tag{8}$$

The expression for the stresses in the adhesive layer is then:

$$\begin{aligned} \sigma^{(a)}_{zz} &= E'^{(a)} \left[\frac{\Delta W^{(a)}}{t^{(a)}} \right] \\ \tau^{(a)}_{xz} &= G'^{(a)} \left[\frac{\Delta U^{(a)}}{t^{(a)}} \right] \\ \tau^{(a)}_{yz} &= G'^{(a)} \left[\frac{\Delta V^{(a)}}{t^{(a)}} \right] \end{aligned} \tag{9}$$

2.3. Governing equations

The equilibrium equations are derived using a variational approach (Mantari and Granados, 2015) applying the virtual work principle:

$$\delta W = \delta W_{int} + \delta W_{ext} = 0 \qquad \forall \delta D \tag{10}$$

where δD are the virtual displacements compatible with the boundary conditions and δW_{int} and δW_{ext} the internal and external virtual work, respectively. In an isolated system with no body forced nor surface traction, δW_{ext} is trivially equal to zero and the expression for the internal virtual work is

$$\begin{aligned} -\delta W_{int} = &\int_\Omega \sigma_{xx} \cdot \delta\varepsilon_{xx}\, d\Omega + \int_\Omega \sigma_{yy} \cdot \delta\varepsilon_{yy}\, d\Omega + \int_\Omega \sigma_{zz} \cdot \delta\varepsilon_{zz}\, d\Omega \\ &+ \int_\Omega \sigma_{xy} \cdot \delta\varepsilon_{xy}\, d\Omega + \int_\Omega \sigma_{xz} \cdot \delta\varepsilon_{xz}\, d\Omega + \int_\Omega \sigma_{yz} \cdot \delta\varepsilon_{yz}\, d\Omega \end{aligned} \tag{11}$$

where Ω is the volume of the solid and the integrands represent the virtual work density exerted by the stress fields.

The principle is applied below to derive the equilibrium equations of the SLJ assembly within the presented framework, both for the bonded and the free regions of the substrates. Since the plates are assumed to be free from body forces, Eq. (10) reduces to the expression of δW_{int}, as the external work is identically zero.

2.3.1. Isolated adherend

The variational form of Eq. (3) can be inserted into Eq. (11) to yield:

$$\begin{aligned} -\delta W^{(s)}_{int} = &\int_{\Omega^{(s)}} \sigma^{(s)}_{xx} \sum_{j=0}^{n^{(s)}_y} \sum_{k=0}^{n^{(s)}_z} \frac{d\delta u^{(s)}_{jk}(x)}{dx} \cdot y^j z^k d\Omega^{(s)} \\ &+ \int_{\Omega^{(s)}} \sigma^{(s)}_{yy} \sum_{j=0}^{m^{(s)}_y} \sum_{k=0}^{m^{(s)}_z} \delta v^{(s)}_{jk}(x) \cdot j y^{j-1} z^k d\Omega^{(s)} \\ &+ \frac{1}{2} \int_{\Omega^{(s)}} \tau^{(s)}_{xy} \left[\sum_{j=0}^{m^{(s)}_y} \sum_{k=0}^{m^{(s)}_z} \frac{d\delta v^{(s)}_{jk}(x)}{dx} \cdot y^j z^k + \sum_{j=0}^{n^{(s)}_y} \sum_{k=0}^{n^{(s)}_z} \delta u^{(s)}_{jk}(x) \cdot j y^{j-1} z^k \right] d\Omega^{(s)} \\ &+ \frac{1}{2} \int_{\Omega^{(s)}} \tau^{(s)}_{xz} \left[\sum_{j=0}^{p^{(s)}_y} \frac{d\delta w^{(s)}_j(x)}{dx} \cdot y^j + \sum_{j=0}^{n^{(s)}_y} \sum_{k=0}^{n^{(s)}_z} \delta u^{(s)}_{jk}(x) \cdot k y^j z^{k-1} \right] d\Omega^{(s)} \\ &+ \frac{1}{2} \int_{\Omega^{(s)}} \tau^{(s)}_{yz} \left[\sum_{j=0}^{p^{(s)}_y} \delta w^{(s)}_j(x) \cdot j y^{j-1} + \sum_{j=0}^{m^{(s)}_y} \sum_{k=0}^{m^{(s)}_z} \delta v^{(s)}_{jk}(x) \cdot k y^j z^{k-1} \right] d\Omega^{(s)} \end{aligned} \tag{12}$$

Integrating by parts and using the notation given by Eq. (6), the internal virtual work can be expressed in a form where it does not depend on the derivatives of the virtual displacement functions as follows:

$$\begin{aligned} -\delta W^{(s)}_{int} = &\sum_{j=0}^{n^{(s)}_y} \sum_{k=0}^{n^{(s)}_z} \left\{ \left[M^{(s)}_{xx,jk} \delta u^{(s)}_{jk}(x) \right]_0^{l^{(s)}} - \int_{l^{(s)}} \frac{dM^{(s)}_{xx,jk}}{dx} \delta u^{(s)}_{jk}(x)\, dx \right\} \\ &+ \sum_{j=0}^{m^{(s)}_y} \sum_{k=0}^{m^{(s)}_z} \int_{l^{(s)}} j M^{(s)}_{yy,(j-1,k)} \delta v^{(s)}_{jk}(x)\, dx \\ &+ \frac{1}{2} \sum_{j=0}^{m^{(s)}_y} \sum_{k=0}^{m^{(s)}_z} \left\{ \left[M^{(s)}_{xy,jk} \delta v^{(s)}_{jk}(x) \right]_0^{l^{(s)}} - \int_{l^{(s)}} \frac{dM^{(s)}_{xy,jk}}{dx} \delta v^{(s)}_{jk}(x) dx \right\} \\ &\quad + \frac{1}{2} \sum_{j=0}^{n^{(s)}_y} \sum_{k=0}^{n^{(s)}_z} \int_{l^{(s)}} j M^{(s)}_{xy,(j-1,k)} \delta u^{(s)}_{jk}(x)\, dx \\ &+ \frac{1}{2} \sum_{j=0}^{p^{(s)}_y} \left\{ \left[M^{(s)}_{xz,(j,0)} \delta w^{(s)}_j(x) \right]_0^{l^{(s)}} - \int_{l^{(s)}} \frac{dM^{(s)}_{xz,(j,0)}}{dx} \delta w^{(s)}_j(x)\, dx \right\} \\ &\quad + \frac{1}{2} \sum_{j=0}^{n^{(s)}_y} \sum_{k=0}^{n^{(s)}_z} \int_{l^{(s)}} k M^{(s)}_{xz,(j,k-1)} \delta u^{(s)}_{jk}(x)\, dx \\ &+ \frac{1}{2} \sum_{j=0}^{p^{(s)}_y} \int_{l^{(s)}} j M^{(s)}_{yz,(j-1,0)} \delta w^{(s)}_j(x)\, dx + \frac{1}{2} \sum_{j=0}^{m^{(s)}_y} \sum_{k=0}^{m^{(s)}_z} \int_{l^{(s)}} k M^{(s)}_{yz,(j,k-1)} \\ &\quad \times \delta v^{(s)}_{jk}(x)\, dx \end{aligned} \tag{13}$$

where $l^{(s)}$ is the length of the isolated plate. From the principle of virtual work (Eq. (10)), since $\delta W_{ext} = 0$, the condition $\delta W_{int} = 0$ must hold for any virtual displacement $\delta u_{jk}^{(s)}(x), \delta v_{jk}^{(s)}(x)$ and $\delta w_j^{(s)}(x)$. This leads to the derivation of the equilibrium equations:

$$\begin{cases} \dfrac{dM_{xx,jk}^{(s)}}{dx} - \frac{1}{2}jM_{xy,(j-1,k)}^{(s)} - \frac{1}{2}kM_{xz,(j,k-1)}^{(s)} = 0, & j = 0,\dots,n_y^{(s)}, \quad k = 0,\dots,n_z^{(s)} \\ \dfrac{dM_{xy,jk}^{(s)}}{dx} - 2jM_{yy,(j-1,k)}^{(s)} - kM_{yz,(j,k-1)}^{(s)} = 0, & j = 0,\dots,m_y^{(s)}, \quad k = 0,\dots,m_z^{(s)} \\ \dfrac{dM_{xz,(j,0)}^{(s)}}{dx} - jM_{yz,(j-1,0)}^{(s)} = 0, & j = 0,\dots,p_y^{(s)} \end{cases} \tag{14}$$

The above differential equations constitute a set of $p_y^{(s)}+1+(n_y^{(s)}+1)\cdot(n_z^{(s)}+1)+(m_y^{(s)}+1)\cdot(m_z^{(s)}+1)$ ordinary differential equations (ODEs), whose dimension depends on the order of development of the series defining the displacement functions. It has been considered, for the sake of simplicity as specified in Section 2.2, that all indices j, k start from zero. This choice does not affect the formulation, since the corresponding terms automatically vanish and do not contribute to the equations.

2.3.2. Bonded overlap

The procedure for deriving the equilibrium equations is analogous to that illustrated for the isolated adherend. However, it requires to express the displacements of the spring ends in terms of those of the adherends, which are kinematically coupled through the elastic foundation.

The virtual internal work of the adhesive is obtained inserting the variational form of the strain–displacement relationships (Eq. (7)) into Eq. (11):

$$\begin{aligned} -\delta W_{int}^{(a)} = &\int_{\Omega^{(a)}} \sigma_{zz}^{(a)} \frac{\Delta\delta W^{(a)}}{t^{(a)}}\, d\Omega^{(a)} + \int_{\Omega^{(a)}} \tau_{xz}^{(a)} \frac{\Delta\delta U^{(a)}}{2t^{(a)}}\, d\Omega^{(a)} \\ &+ \int_{\Omega^{(a)}} \tau_{yz}^{(a)} \frac{\Delta\delta V^{(a)}}{2t^{(a)}}\, d\Omega^{(a)} \end{aligned} \tag{15}$$

The load transfer in the bonded overlap occurs through the forces generated in the springs which, due to the assumption of linear behavior, only depend on the distance between their extremities. This characteristic is exploited to impose the kinematic coupling between the substrates, by equating the displacements of the spring ends to those of the adherend–adhesive interfaces. Specifically, referring to Fig. 2, these correspond to the lower surface of the upper adherend and the upper surface of the lower adherend. Let the upper adherend be denoted by number "1" and the lower by number "2". The coupling condition through the elastic foundation can be therefore written as:

$$\begin{aligned} U_{sup}^{(a)} &= \sum_{j=0}^{n_y^{(1)}}\sum_{k=0}^{n_z^{(1)}} u_{jk}^{(1)}(x)\cdot y^j \left(-\frac{t^{(1)}}{2}\right)^k & U_{inf}^{(a)} &= \sum_{j=0}^{n_y^{(2)}}\sum_{k=0}^{n_z^{(2)}} u_{jk}^{(2)}(x)\cdot y^j \left(\frac{t^{(2)}}{2}\right)^k \\ V_{sup}^{(a)} &= \sum_{j=0}^{m_y^{(1)}}\sum_{k=0}^{m_z^{(1)}} v_{jk}^{(1)}(x)\cdot y^j \left(-\frac{t^{(1)}}{2}\right)^k & V_{inf}^{(a)} &= \sum_{j=0}^{m_y^{(2)}}\sum_{k=0}^{m_z^{(2)}} v_{jk}^{(2)}(x)\cdot y^j \left(\frac{t^{(2)}}{2}\right)^k \\ W_{sup}^{(a)} &= \sum_{j=0}^{p_y^{(1)}} w_j^{(1)}(x)\cdot y^j & W_{inf}^{(a)} &= \sum_{j=0}^{p_y^{(2)}} w_j^{(2)}(x)\cdot y^j \end{aligned} \tag{16}$$

The insertion of the variational form of Eq. (16) into Eq. (15) gives a new expression for the internal virtual work of the adhesive layer, defined in terms of the virtual displacements of the adherends at the interfaces:

$$\begin{aligned} -\delta W_{int}^{(a)} = &\int_{\Omega^{(a)}} \frac{\sigma_{zz}^{(a)}}{t^{(a)}} \left[\sum_{j=0}^{p_y^{(1)}} \delta w_j^{(1)}(x)\cdot y^j - \sum_{j=0}^{p_y^{(2)}} \delta w_j^{(2)}(x)\cdot y^j\right] d\Omega^{(a)} \\ &+ \int_{\Omega^{(a)}} \frac{\tau_{xz}^{(a)}}{2t^{(a)}} \left[\sum_{j=0}^{n_y^{(1)}}\sum_{k=0}^{n_z^{(1)}} \delta u_{jk}^{(1)}(x)\cdot y^j \left(-\frac{t^{(1)}}{2}\right)^k \right. \\ &\left. - \sum_{j=0}^{n_y^{(2)}}\sum_{k=0}^{n_z^{(2)}} \delta u_{jk}^{(2)}(x)\cdot y^j \left(\frac{t^{(2)}}{2}\right)^k\right] d\Omega^{(a)} \\ &+ \int_{\Omega^{(a)}} \frac{\tau_{yz}^{(a)}}{2t^{(a)}} \left[\sum_{j=0}^{m_y^{(1)}}\sum_{k=0}^{m_z^{(1)}} \delta v_{jk}^{(1)}(x)\cdot y^j \left(-\frac{t^{(1)}}{2}\right)^k \right. \\ &\left. - \sum_{j=0}^{m_y^{(2)}}\sum_{k=0}^{m_z^{(2)}} \delta v_{jk}^{(2)}(x)\cdot y^j \left(\frac{t^{(2)}}{2}\right)^k\right] d\Omega^{(a)} \end{aligned} \tag{17}$$

Since no derivatives of the virtual displacements are involved, no integration by parts is needed. The notations given by Eq. (6) are then applied so that

$$\begin{aligned} -\delta W_{int}^{(a)} = &\sum_{j=0}^{p_y^{(1)}} \int_{l^{(a)}} \frac{M_{zz,(j,0)}^{(a)}}{t^{(a)}} \delta w_j^{(1)}(x)\, dx - \sum_{j=0}^{p_y^{(2)}} \int_{l^{(a)}} \frac{M_{zz,(j,0)}^{(a)}}{t^{(a)}} \delta w_j^{(2)}(x)\, dx \\ &+ \sum_{j=0}^{n_y^{(1)}}\sum_{k=0}^{n_z^{(1)}} (-1)^k \int_{l^{(a)}} \frac{M_{xz,(j,0)}^{(a)}}{2t^{(a)}} \delta u_{jk}^{(1)}(x) \left(\frac{t^{(1)}}{2}\right)^k dx \\ &+ \sum_{j=0}^{n_y^{(2)}}\sum_{k=0}^{n_z^{(2)}} (-1) \int_{l^{(a)}} \frac{M_{xz,(j,0)}^{(a)}}{2t^{(a)}} \delta u_{jk}^{(2)}(x) \left(\frac{t^{(2)}}{2}\right)^k dx \\ &+ \sum_{j=0}^{m_y^{(1)}}\sum_{k=0}^{m_z^{(1)}} (-1)^k \int_{l^{(a)}} \frac{M_{yz,(j,0)}^{(a)}}{2t^{(a)}} \delta v_{jk}^{(1)}(x) \left(\frac{t^{(1)}}{2}\right)^k dx \\ &+ \sum_{j=0}^{m_y^{(2)}}\sum_{k=0}^{m_z^{(2)}} (-1) \int_{l^{(a)}} \frac{M_{yz,(j,0)}^{(a)}}{2t^{(a)}} \delta v_{jk}^{(2)}(x) \left(\frac{t^{(2)}}{2}\right)^k dx \end{aligned} \tag{18}$$

where $l^{(a)}$ is the overlap length.

In the bonded overlap region, the total virtual work consists of the contributions of both the two adherents and the adhesive. The principle of virtual work, considering that the body and surface forces are zero, is thus written as

$$\delta W = \delta W_{int} + \delta W_{ext} = \delta W_{int}^{(1)} + \delta W_{int}^{(2)} + \delta W_{int}^{(a)} = 0 \qquad \forall \delta U \tag{19}$$

From Eq. (19), the condition that δW must vanish for every virtual displacement $\delta u_{jk}^{(1)}(x)$, $\delta u_{jk}^{(2)}(x), \delta v_{jk}^{(1)}(x), \delta v_{jk}^{(2)}(x), \delta w_j^{(1)}(x)$ and $\delta w_j^{(2)}(x)$ leads to the equilibrium equations:

$$
\begin{cases}
\dfrac{dM^{(1)}_{xx,jk}}{dx} - \frac{1}{2}jM^{(1)}_{xy,(j-1,k)} - \frac{1}{2}kM^{(1)}_{xz,(j,k-1)} \\
\quad + \dfrac{(-1)^{k+1}}{2t^{(a)}}\left(\dfrac{t^{(1)}}{2}\right)^k M^{(a)}_{xz,(j,0)} = 0, & j = 0,\dots,n^{(1)}_y,\ k = 0,\dots,n^{(1)}_z \\
\dfrac{dM^{(2)}_{xx,jk}}{dx} - \frac{1}{2}jM^{(2)}_{xy,(j-1,k)} - \frac{1}{2}kM^{(2)}_{xz,(j,k-1)} \\
\quad + \dfrac{1}{2t^{(a)}}\left(\dfrac{t^{(2)}}{2}\right)^k M^{(a)}_{xz,(j,0)} = 0, & j = 0,\dots,n^{(2)}_y,\ k = 0,\dots,n^{(2)}_z \\
\dfrac{dM^{(1)}_{xy,jk}}{dx} - 2jM^{(1)}_{yy,(j-1,k)} - kM^{(1)}_{yz,(j,k-1)} \\
\quad + \dfrac{(-1)^{k+1}}{t^{(a)}}\left(\dfrac{t^{(1)}}{2}\right)^k M^{(a)}_{yz,(j,0)} = 0, & j = 0,\dots,m^{(1)}_y,\ k = 0,\dots,m^{(1)}_z \\
\dfrac{dM^{(2)}_{xy,jk}}{dx} - 2jM^{(2)}_{yy,(j-1,k)} - kM^{(2)}_{yz,(j,k-1)} \\
\quad + \dfrac{1}{t^{(a)}}\left(\dfrac{t^{(2)}}{2}\right)^k M^{(a)}_{yz,(j,0)} = 0, & j = 0,\dots,m^{(2)}_y,\ k = 0,\dots,m^{(2)}_z \\
\dfrac{dM^{(1)}_{xz,(j,0)}}{dx} - jM^{(1)}_{yz,(j-1,0)} \\
\quad - \dfrac{2}{t^{(a)}}M^{(a)}_{zz,(j,0)} = 0, & j = 0,\dots,p^{(1)}_y \\
\dfrac{dM^{(2)}_{xz,(j,0)}}{dx} - jM^{(2)}_{yz,(j-1,0)} \\
\quad + \dfrac{2}{t^{(a)}}M^{(a)}_{zz,(j,0)} = 0, & j = 0,\dots,p^{(2)}_y
\end{cases}
\tag{20}
$$

The differential equations presented above constitute a set of $p^{(1)}_y + p^{(2)}_y + 2 + (n^{(1)}_y + 1)\cdot(n^{(1)}_z + 1) + (n^{(2)}_y + 1)\cdot(n^{(2)}_z + 1) + (m^{(1)}_y + 1)\cdot(m^{(1)}_z + 1) + (m^{(2)}_y + 1)\cdot(m^{(2)}_z + 1)$ ODEs. If the same kinematics are assumed for both adherends, i.e. the same higher-order term in the displacement function series, then the number of equilibrium equations for the bonded overlap will be twice that of the isolated adherend.

2.4. Stiffness matrix

Two systems of differential equilibrium equations have been determined for the isolated (Eq. (14)) and bonded (Eq. (20)) regions of a SLJ.

2.4.1. Equilibrium equations solution

By progressively substituting the definitions of the numerical internal moments (Eq. (6)), the stress–strain relationships (Eq. (5)) and the strain–displacement relations (Eq. (3)) into the equilibrium equations, and finally evaluating the integrals, it is possible to rewrite the equilibrium equations in terms of the displacement functions. It can be verified that the expression for each internal numerical moment of fixed $\bar{j},\bar{k}$ order in terms of displacement functions for the sth adherend is:

$$
\begin{aligned}
M^{(s)}_{xx,\bar{j}\bar{k}} = {} & E'^{(s)}\sum_{j=0}^{n^{(s)}_y}\sum_{k=0}^{n^{(s)}_z}\frac{du^{(s)}_{jk}(x)}{dx}\cdot\frac{1+(-1)^{j+\bar{j}}}{j+\bar{j}+1}\left(\frac{b^{(s)}}{2}\right)^{j+\bar{j}+1} \\
& \cdot\frac{1+(-1)^{k+\bar{k}}}{k+\bar{k}+1}\left(\frac{t^{(s)}}{2}\right)^{k+\bar{k}+1} \\
& + \nu'^{(s)}E'^{(s)}\sum_{j=0}^{m^{(s)}_y}\sum_{k=0}^{m^{(s)}_z}v^{(s)}_{jk}(x)\cdot j\cdot\frac{1+(-1)^{j+\bar{j}-1}}{j+\bar{j}}\left(\frac{b^{(s)}}{2}\right)^{j+\bar{j}} \\
& \cdot\frac{1+(-1)^{k+\bar{k}}}{k+\bar{k}+1}\left(\frac{t^{(s)}}{2}\right)^{k+\bar{k}+1}
\end{aligned}
$$

$$
\begin{aligned}
M^{(s)}_{yy,\bar{j}\bar{k}} = {} & \nu'^{(s)}E'^{(s)}\sum_{j=0}^{n^{(s)}_y}\sum_{k=0}^{n^{(s)}_z}\frac{du^{(s)}_{jk}(x)}{dx}\cdot\frac{1+(-1)^{j+\bar{j}}}{j+\bar{j}+1}\left(\frac{b^{(s)}}{2}\right)^{j+\bar{j}+1} \\
& \cdot\frac{1+(-1)^{k+\bar{k}}}{k+\bar{k}+1}\left(\frac{t^{(s)}}{2}\right)^{k+\bar{k}+1} \\
& + E'^{(s)}\sum_{j=0}^{m^{(s)}_y}\sum_{k=0}^{m^{(s)}_z}v^{(s)}_{jk}(x)\cdot j\cdot\frac{1+(-1)^{j+\bar{j}-1}}{j+\bar{j}}\left(\frac{b^{(s)}}{2}\right)^{j+\bar{j}} \\
& \cdot\frac{1+(-1)^{k+\bar{k}}}{k+\bar{k}+1}\left(\frac{t^{(s)}}{2}\right)^{k+\bar{k}+1}
\end{aligned}
$$

$$
\begin{aligned}
M^{(s)}_{xy,\bar{j}\bar{k}} = {} & G'^{(s)}\sum_{j=0}^{m^{(s)}_y}\sum_{k=0}^{m^{(s)}_z}\frac{dv^{(s)}_{jk}(x)}{dx}\cdot\frac{1+(-1)^{j+\bar{j}}}{j+\bar{j}+1}\left(\frac{b^{(s)}}{2}\right)^{j+\bar{j}+1} \\
& \cdot\frac{1+(-1)^{k+\bar{k}}}{k+\bar{k}+1}\left(\frac{t^{(s)}}{2}\right)^{k+\bar{k}+1} \\
& + G'^{(s)}\sum_{j=0}^{n^{(s)}_y}\sum_{k=0}^{n^{(s)}_z}u^{(s)}_{jk}(x)\cdot j\cdot\frac{1+(-1)^{j+\bar{j}-1}}{j+\bar{j}}\left(\frac{b^{(s)}}{2}\right)^{j+\bar{j}} \\
& \cdot\frac{1+(-1)^{k+\bar{k}}}{k+\bar{k}+1}\left(\frac{t^{(s)}}{2}\right)^{k+\bar{k}+1}
\end{aligned}
$$

$$
\begin{aligned}
M^{(s)}_{xz,\bar{j}\bar{k}} = {} & G'^{(s)}\sum_{j=0}^{p^{(s)}_y}\frac{dw^{(s)}_{j}(x)}{dx}\cdot\frac{1+(-1)^{j+\bar{j}}}{j+\bar{j}+1}\left(\frac{b^{(s)}}{2}\right)^{j+\bar{j}+1} \\
& \cdot\frac{1+(-1)^{\bar{k}}}{\bar{k}+1}\left(\frac{t^{(s)}}{2}\right)^{\bar{k}+1} \\
& + G'^{(s)}\sum_{j=0}^{n^{(s)}_y}\sum_{k=0}^{n^{(s)}_z}u^{(s)}_{jk}(x)\cdot k\cdot\frac{1+(-1)^{j+\bar{j}}}{j+\bar{j}+1}\left(\frac{b^{(s)}}{2}\right)^{j+\bar{j}+1} \\
& \cdot\frac{1+(-1)^{k+\bar{k}-1}}{k+\bar{k}}\left(\frac{t^{(s)}}{2}\right)^{k+\bar{k}}
\end{aligned}
$$

$$
\begin{aligned}
M^{(s)}_{yz,\bar{j}\bar{k}} = {} & G'^{(s)}\sum_{j=0}^{p^{(s)}_y}w^{(s)}_{j}(x)\cdot j\cdot\frac{1+(-1)^{j+\bar{j}-1}}{j+\bar{j}}\left(\frac{b^{(s)}}{2}\right)^{j+\bar{j}} \\
& \cdot\frac{1+(-1)^{\bar{k}}}{\bar{k}+1}\left(\frac{t^{(s)}}{2}\right)^{\bar{k}+1} \\
& + G'^{(s)}\sum_{j=0}^{m^{(s)}_y}\sum_{k=0}^{m^{(s)}_z}v^{(s)}_{jk}(x)\cdot k\cdot\frac{1+(-1)^{j+\bar{j}}}{j+\bar{j}+1}\left(\frac{b^{(s)}}{2}\right)^{j+\bar{j}+1} \\
& \cdot\frac{1+(-1)^{k+\bar{k}-1}}{k+\bar{k}}\left(\frac{t^{(s)}}{2}\right)^{k+\bar{k}}
\end{aligned}
\tag{21}
$$

where the positioning of the reference system of Fig. 1, centered at half-width and half-thickness of the plate, is exploited, so that the integrals of odd functions over the y and z directions vanish. The same can be ascertained for the internal numerical moments of the adhesive layer making use of the stress–displacement relations Eq. (9) and considering the coupling condition of Eq. (16), leading to:

$$
\begin{aligned}
M^{(a)}_{xz,(\bar{j},0)} = {} & G'^{(a)}\sum_{j=0}^{n^{(1)}_y}\sum_{k=0}^{n^{(1)}_z}u^{(1)}_{jk}(x)\cdot(-1)^k\left(\frac{t^{(1)}}{2}\right)^k\cdot\frac{1+(-1)^{j+\bar{j}}}{j+\bar{j}+1}\left(\frac{b^{(a)}}{2}\right)^{j+\bar{j}+1} \\
& - G'^{(a)}\sum_{j=0}^{n^{(2)}_y}\sum_{k=0}^{n^{(2)}_z}u^{(2)}_{jk}(x)\cdot\left(\frac{t^{(2)}}{2}\right)^k\cdot\frac{1+(-1)^{j+\bar{j}}}{j+\bar{j}+1}\left(\frac{b^{(a)}}{2}\right)^{j+\bar{j}+1}
\end{aligned}
$$

$$
\begin{aligned}
M^{(a)}_{yz,(\bar{j},0)} = {} & G'^{(a)}\sum_{j=0}^{m^{(1)}_y}\sum_{k=0}^{m^{(1)}_z}v^{(1)}_{jk}(x)\cdot(-1)^k\left(\frac{t^{(1)}}{2}\right)^k\cdot\frac{1+(-1)^{j+\bar{j}}}{j+\bar{j}+1}\left(\frac{b^{(a)}}{2}\right)^{j+\bar{j}+1} \\
& - G'^{(a)}\sum_{j=0}^{m^{(2)}_y}\sum_{k=0}^{m^{(2)}_z}v^{(2)}_{jk}(x)\cdot\left(\frac{t^{(2)}}{2}\right)^k\cdot\frac{1+(-1)^{j+\bar{j}}}{j+\bar{j}+1}\left(\frac{b^{(a)}}{2}\right)^{j+\bar{j}+1}
\end{aligned}
$$

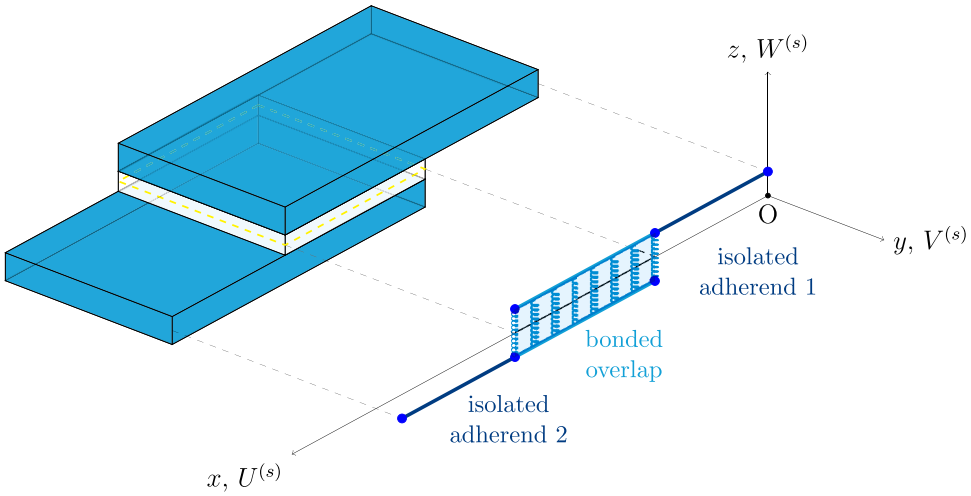

Fig. 3. ME modeling of SLJ assembly.

$$M^{(a)}_{zz,(\bar{j},0)} = E'^{(a)} \sum_{j=0}^{p_y^{(1)}} w_j^{(1)}(x) \cdot \frac{1+(-1)^{j+\bar{j}}}{j+\bar{j}+1} \left(\frac{b^{(a)}}{2}\right)^{j+\bar{j}+1} - E'^{(a)} \sum_{j=0}^{p_y^{(2)}} w_j^{(2)}(x) \cdot \frac{1+(-1)^{j+\bar{j}}}{j+\bar{j}+1} \left(\frac{b^{(a)}}{2}\right)^{j+\bar{j}+1} \tag{22}$$

The systems of equilibrium equations Eqs. (14) and (20), once expressed in terms of displacement functions via Eqs. (21) and (22), constitute sets of second-order linear ODEs dependent only on the x variable. As is well known, a system of this kind, comprising N second-order equations, can be recast as an equivalent system of $2N$ first-order linear ODEs. Introducing N auxiliary equations, the set can be effectively represented in a matrix form as:

$$\frac{dY(x)}{dx} = AY(x) \tag{23}$$

where A is a square matrix of size $2N \times 2N$ and $Y(x)$ is the vector collecting the unknown functions and their first derivatives.

For the problem under consideration, let $q(x)$ be a vector that contains all the individual displacement functions $u^{(s)}_{jk}(x), v^{(s)}_{jk}(x)$ and $w^{(s)}_j(x)$. In light of the above, the equilibrium equations systems for both the isolated (Eq. (14)) and bonded (Eq. (20)) regions of a SLJ can be written in the form of Eq. (23), where

$$Y(x) = \left\{ q(x) \quad \frac{dq(x)}{dx} \right\}^T \qquad \frac{dY(x)}{dx} = \left\{ \frac{dq(x)}{dx} \quad \frac{d^2q(x)}{dx^2} \right\}^T \tag{24}$$

A classical solution for this problem, already tested in Schwartz et al. (2020), is:

$$Y(x) = e^{A \cdot x} \cdot C \tag{25}$$

where the expression consists of the matrix exponential of $A \cdot x$ and a vector of integration constants C. The complete displacement field of the bonded assembly can be then reconstructed by extracting the displacement functions in $q(x)$ from $Y(x)$ and inserting them into the series expansions of Eq. (1).

2.4.2. Numerical implementation

The solution requires the determination of the integration constants of C. One of the key advantages of the ME methodology presented is that it can be integrated into the standard structure of a FEM solving algorithm, where the relationship between nodal forces and displacement is expressed through the classical equation, derived from the minimization of the potential energy:

$$F = K \cdot U \tag{26}$$

where K is the stiffness matrix. In this framework, the SLJ assembly can be discretized into three ME, one for each isolated portion of the two adherends and one for the bonded region, as shown in Fig. 3. The vectors of nodal displacements and loads, denoted by U and F respectively, can be calculated as:

$$U = D \cdot C \qquad F = L \cdot C \tag{27}$$

where D and L are square matrices that can be determined based on the boundary conditions assigned and the geometric and material characteristics of the assembly. Substituting Eq. (27) into Eq. (26) and rearranging the expression, it is finally possible to determine the stiffness matrix K of the ME as:

$$K = L \cdot D^{-1} \tag{28}$$

Table 1
Geometric parameters of the SLJ test case designed according to ASTM D1002-10.

$l^{(1)}$ [mm]	$l^{(2)}$ [mm]	$l^{(a)}$ [mm]	$t^{(1)}$ [mm]	$t^{(2)}$ [mm]	$t^{(a)}$ [mm]	b [mm]
63.5	63.5	25.4	1.6	1.6	0.25	25.4

3. Results on the single-lap joint

3.1. Case study

The presented ME formulation was implemented and confronted with a FE model for the test case of a SLJ. The virtual experiment was designed according to the standard ASTM D1002-10 (ASTM, 2019) and is illustrated in Fig. 4. The dimensions of the specimen are reported in Table 1, where b is the sample width, t the thickness, l the adherend free and overlap lengths and the superscripts $1, 2, a$ respectively refer to the first, second adherend and adhesive.

The materials selected are aluminium 6061-T6 for the adherends, a commonly used alloy in aerospace applications, and the structural epoxy adhesive 3M Scotch-Weld™AF 163-2K. Both materials are assumed to be homogeneous and isotropic, and their behavior is supposed to be linear elastic. Their characteristics are detailed in Table 2.

A static tensile load of 1000 N is applied in longitudinal direction at the center of the assembly.

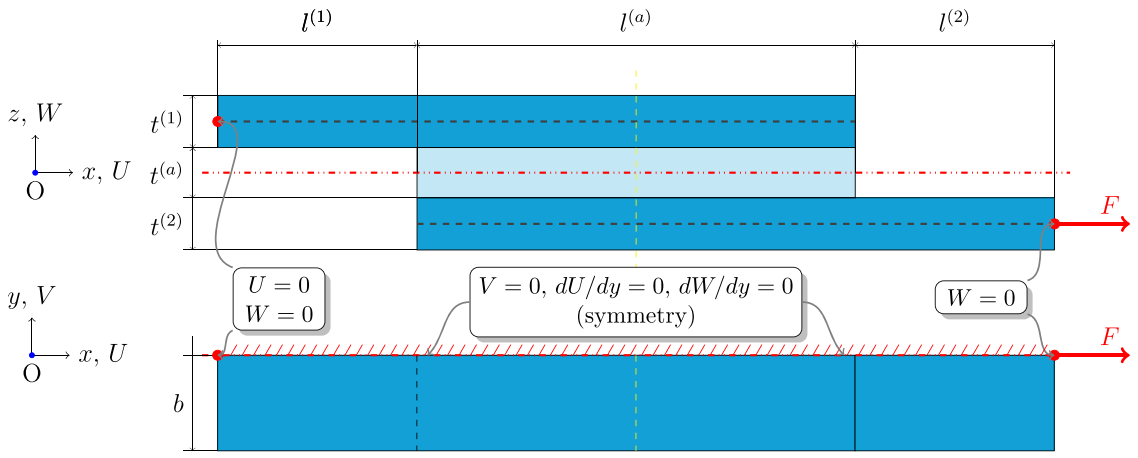

Fig. 4. 3D FE virtual experiment model.

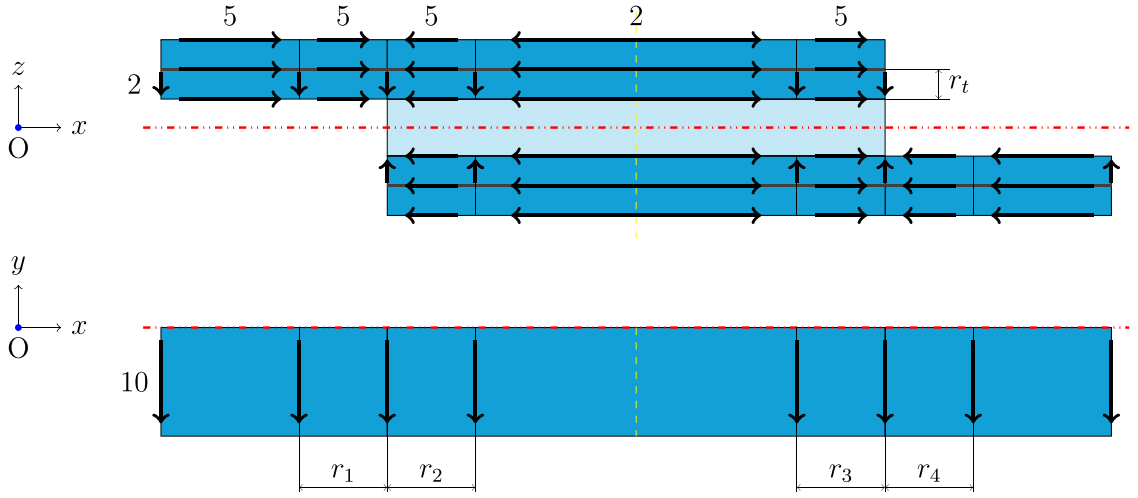

Fig. 5. 3D FE model domain subdivision and refinements. The arrows indicate the direction of decreasing element size, the corresponding numbers indicate the bias.

Table 2
Material properties of aluminium 6061-T6 and adhesive AF 163-2K (Teixeira de Freitas and Sinke, 2017).

$E^{(1)}$ [MPa]	$\nu^{(1)}$	$E^{(2)}$ [MPa]	$\nu^{(2)}$	$E^{(a)}$ [MPa]	$\nu^{(a)}$
68 900	0.33	68 900	0.33	2043	0.34

Table 3
Dimensions of subdomains for meshing strategy.

r_1 [mm]	r_2 [mm]	r_3 [mm]	r_4 [mm]	$r_{t^{(s)}}$
4.5	4.5	4.5	4.5	$t^{(s)}/2$

3.2. 3D FE model

A 3D FE model was created with the ABAQUS 2022 software as shown in Fig. 4. Eight-node linear brick elements with full integration and six degrees of freedom per node (C3D8) were used for both the adherends and the adhesive. To reduce computational cost, only half width of the SLJ was modeled, assigning a symmetry constraint on its midplane. As a consequence, the applied load in the FE model was halved (500 N). The boundary conditions were imposed on reference points located at the mid-thickness of the plate free ends on the symmetry plane, which were then connected to the plates via a kinematic coupling. The simple support constraint is commonly adopted in the literature (He, 2011), as it typically does not affect the behavior of the overlap, provided that the free length of the adherends is sufficiently large. The SLJ was simulated as a single continuous part, rather than multiple bodies with kinematic couplings, by assigning the material characteristics in Table 2 to the respective regions.

To further reduce the number of elements while ensuring convergence of the solution, a parametric meshing strategy was implemented. Multiple refinements were applied based on the number of elements through the adhesive thickness, which was discretized with uniformly spaced seeds in the through-thickness direction. To assign the refinements with a smooth transition in element size, the structure was divided into subdomains, as illustrated in Fig. 5 and detailed in Table 3. Parallel edges share the same bias and the same strategy is applied to both adherends. This scheme also entails that the smallest elements of the mesh are those positioned at the interface and free edge of the SLJ, and are cubic. This approach guarantees accuracy in critical areas subjected to high stress gradients. A picture of the resulting mesh is shown in Fig. 6.

The mesh convergence was verified varying the number of elements in the adhesive thickness and examining the stresses on the path identified by the intersection of the adhesive midplane and the symmetry plane. The result is illustrated in Fig. 7, with the convergence being attained for 8 elements.

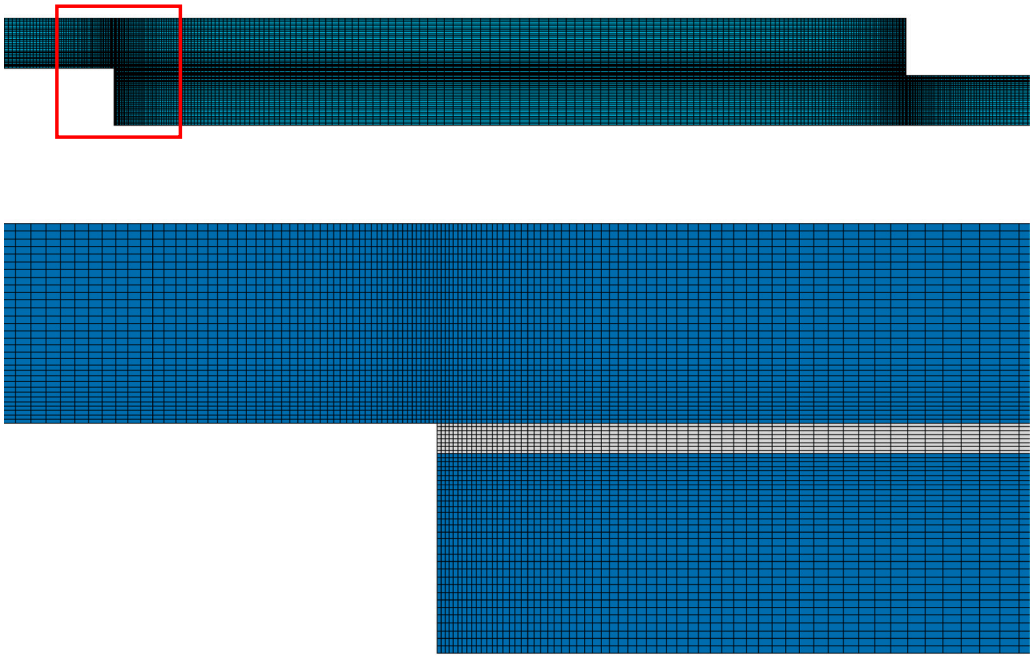

Fig. 6. 3D FE mesh illustration with zoomed detail in ABAQUS 2022.

3.3. Comparison and discussion

The results of the FE and ME analyses were compared under various assumptions to validate the simplified stress analysis of the SLJ. The same expansion orders were applied to both adherends.

3.3.1. Classic theories

As explained in Section 2.2, standard plate theories can be recovered from the presented high-order formulation by introducing the assumption of cylindrical bending and neglecting the y-coordinate dependence of the displacement field. The Reissner–Mindlin and Reddy theories were implemented in the ME framework by selecting $(n_z^{(s)}, m_z^{(s)}) = (1,1)$ and $(3,3)$, respectively, while $n_y^{(s)}, m_y^{(s)}$ and $p_y^{(s)}$ were set to zero. The moduli E' and ν' were initially assumed to be equal to those indicated in Table 2, with the shear moduli calculated as $G' = E'/(2(1+\nu'))$. The results presented were used for the verification of the model.

The stresses in the adhesive layer in the longitudinal direction are shown in Fig. 8. First, the general shape of the stress distributions along the overlap aligns with the expected physical behavior of the problem, exhibiting a near-zero stress region at the center and a sharp concentration towards the ends of the overlap. The zero value of τ_{yz} is consistent with the assumption of cylindrical bending, as the transverse displacement $V^{(s)}$ is constant through the width. This feature also implies that all the stresses are constant in the y direction at the same x coordinate. The zero-stress condition at the overlap free ends is not satisfied as a consequence of the elastic foundation model. However, the formulation still allows for an effective estimation of the peak values in their immediate vicinity. Moreover, this outcome may also be considered representative of a real joint, where some residual load is transferred by the spew fillets (Mortensen and Thomsen, 2002). Secondly, the solutions calculated under the Reissner–Mindlin and Reddy assumptions are nearly indistinguishable. This result is consistent with the study case of a thin plate, whereas more significant differences would be expected for thicker plates. Finally, the maximum stresses are predicted with good accuracy and only slight underestimation. The non-zero value of τ_{yz} resulting from the FE is likely only a computational residual, given its extremely small value.

The proposed methodology also allows to fully reconstruct the entire displacement, strain and stress fields in the adherends. Contour plots of the longitudinal stress σ_{xx} are shown in Fig. 9, while the corresponding difference with respect to the FE reference is depicted in Fig. 10. Broad agreement is shown across the entire plate, with a reasonable estimation of the extreme values. The areas of stress concentration at the overlap left-end corners are correctly identified, and the error magnitude is small compared to the local stress intensity.

3.3.2. Y-coordinate dependence

The cylindrical bending assumption was removed in order to investigate the full three-dimensional formulation of the ME model. Based on the aforementioned results, a Reissner–Mindlin-type kinematics was retained for the z-coordinate dependence of the model by fixing $(n_z^{(s)}, m_z^{(s)}) = (1,1)$. Meanwhile, the expansion orders relative to the y-coordinate - $n_y^{(s)}, m_y^{(s)}$ and $p_y^{(s)}$ - were varied jointly from 0 to 3.

The results of the analysis are shown in Fig. 11. While the global shape of the solution remains consistent with FE, the inclusion of the third dimension dependence improves the accuracy of the maximum stress predictions in the adhesive layer. In particular, the first-order expansion $(n_y, m_y, p_y = 1)$ introduces an increase in the stresses due to the coupling between deformations and Poisson effect. The first-order displacement field, however, does not directly affect the solution since it is associated with an odd function, whilst the loading and boundary conditions are symmetric. The even second-order expansion $(n_y, m_y, p_y = 2)$, instead, is activated by the loading condition, significantly improving the stress prediction for σ_{zz} and τ_{xz}. The third-order expansion $(n_y, m_y, p_y = 3)$, in line with the above analysis, does not influence the solution further. In the context of the present study case, second-order expansion constitutes the most representative kinematic description and provides the best correlation with the FE results.

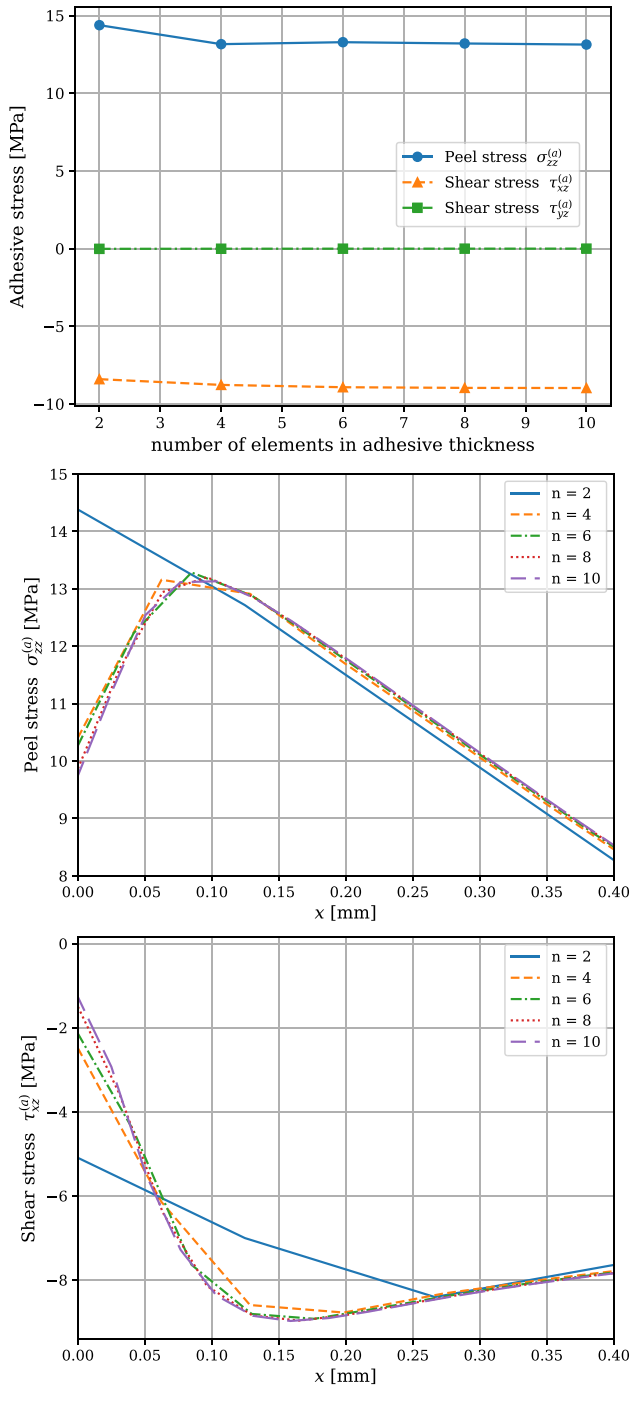

Fig. 7. Convergence analysis for the mesh of the FE model.

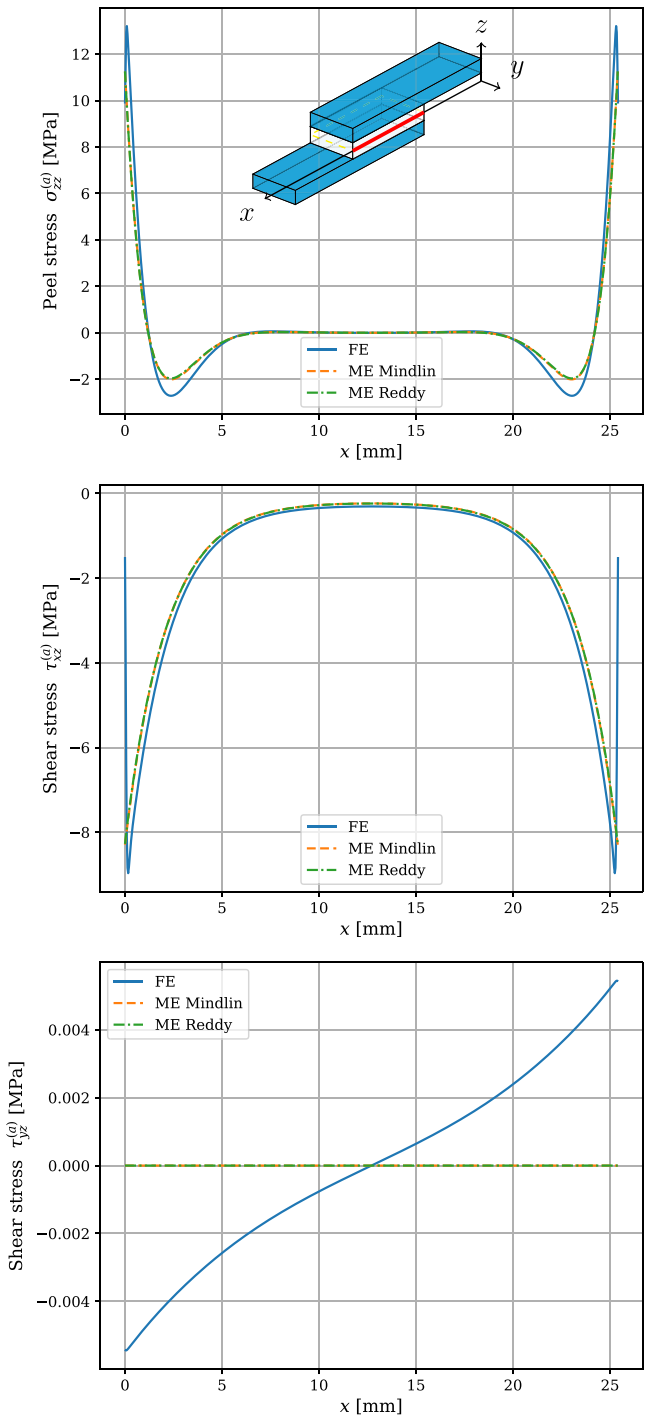

Fig. 8. FE and ME adhesive stresses for different classic plate theories in cylindrical bending along the symmetry plane in the longitudinal direction.

The influence of three-dimensional kinematics on the adhesive stress can be better illustrated by analyzing the displacement fields in the adherends. The inclusion of the y-coordinate dependence allows to model the striction of the substrates in the transversal direction at the adherend-adhesive interface, which alters the adhesive stress state. This behavior is purely 3D and cannot be reproduced by classical two-dimensional models. The transversal displacement V is shown in Figs. 12 and 13 on the yz and xy planes, respectively, for a Reissner–Mindlin-type kinematics with second-order dependence on the y-coordinate.

The contours in Fig. 12 represent a through-thickness slice of the upper adherend taken at the left end of the overlap. The shape of the field is correctly captured, with a more pronounced contraction near the corners at the adhesive interface and a milder elongation on the top surface. Despite the positive effect on the adhesive stress prediction, local displacement values may still exhibit some numerical inaccuracies.

The contours in Fig. 13 correspond to a midplane slice of the upper adherend across the entire overlap length and width. Unlike the previous case, the displacement field is accurately predicted only

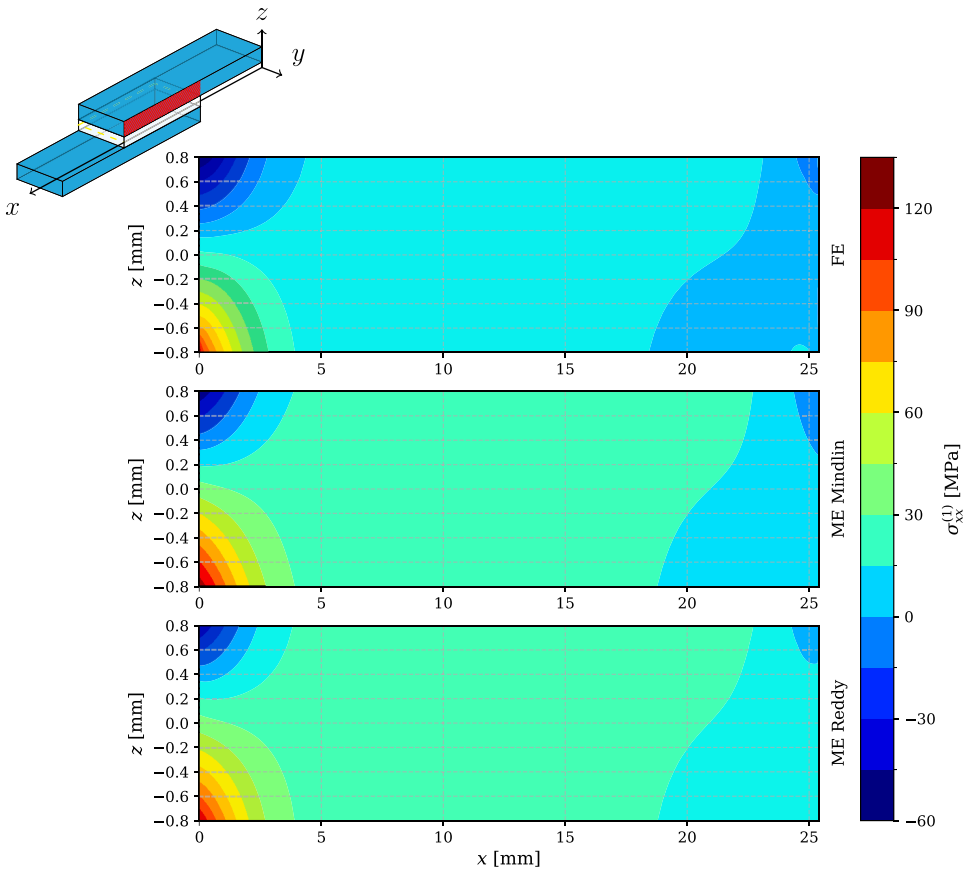

Fig. 9. Contours of FE and ME upper adherend longitudinal stress on the symmetry plane in the overlap region for different classic plate theories in cylindrical bending.

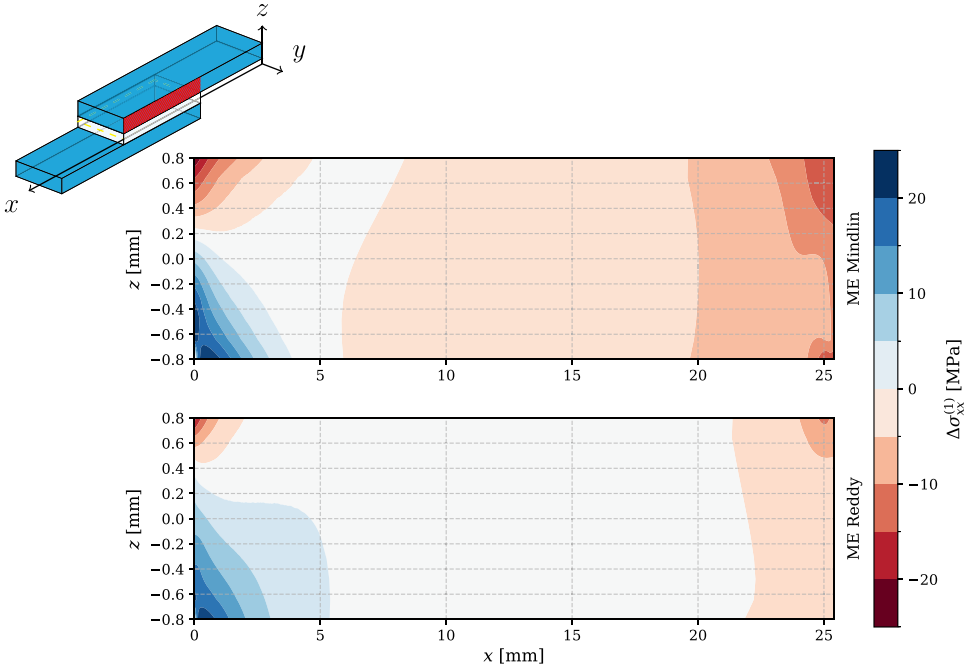

Fig. 10. Contours of ME upper adherend longitudinal stress difference with respect to FE on the symmetry plane in the overlap region for different classic plate theories in cylindrical bending.

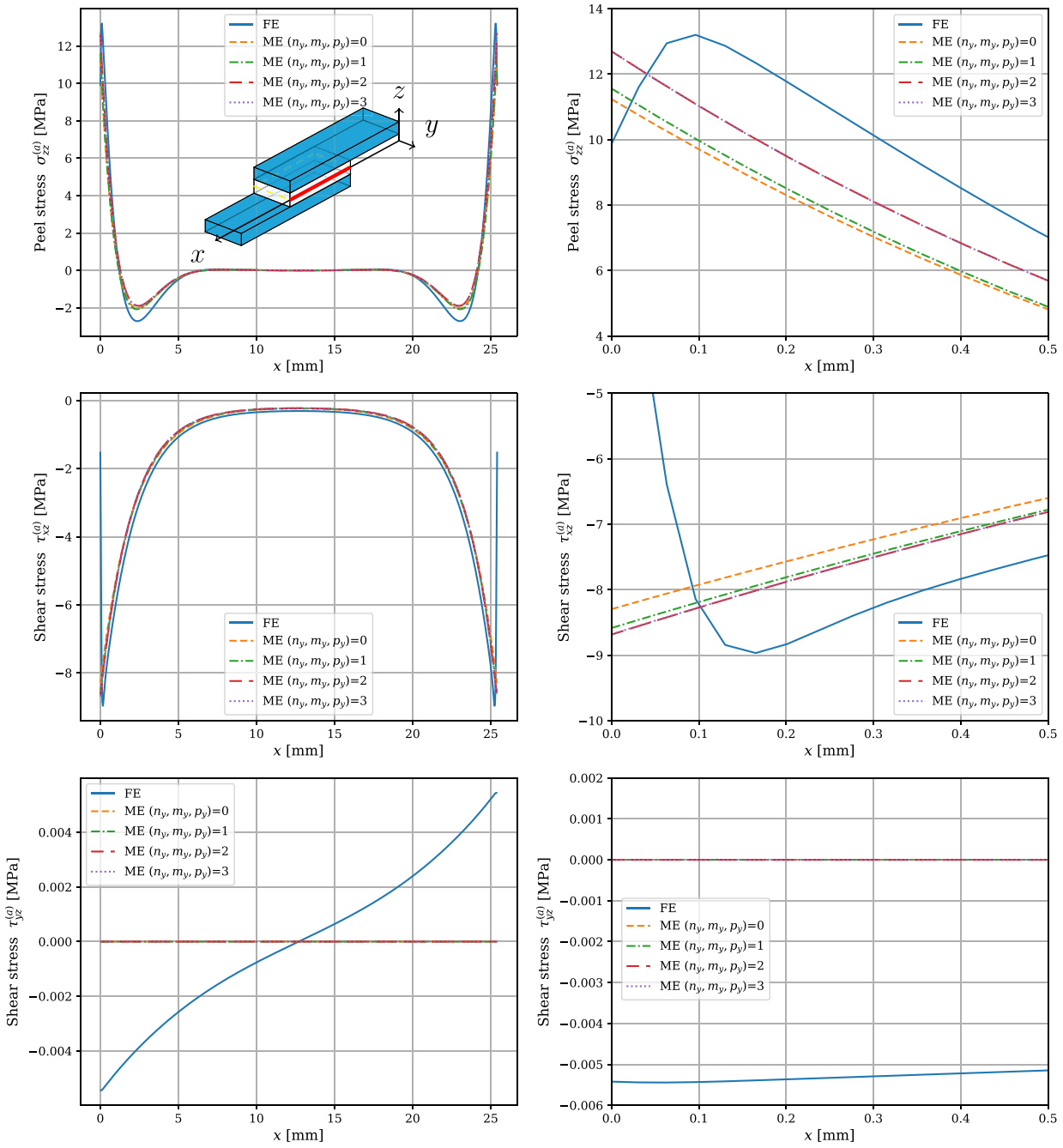

Fig. 11. FE and ME adhesive stresses for different expansion orders of y kinematics along the symmetry plane in the longitudinal direction with zooms.

on the left side of the overlap, while the right one is not correctly represented. This discrepancy arises because the left end is mechanically connected to the rest of the substrate, whereas the right end is free and responds only to the action of the underlying adhesive. As previously discussed, the elastic foundation model fails to reproduce the adhesive zero-stress condition at free edges, and rather predicts maximum stress values there, affecting the results in the right end free corners. Nevertheless, these localized inaccuracies do not compromise the overall improvement in adhesive stress prediction.

These findings form the basis for the validation of the newly presented methodology. The representation of three-dimensional transverse effects provides a substantial improvement in the stress analysis of bonded joints and highlights the potential of ME as a computationally efficient alternative to FE.

3.3.3. Constitutive models

As discussed in Section 2.2, the notation introduced in Eq. (5) allows for easy modification of the constitutive relations to account for various models or effects, such as the confinement of the adhesive or the assumptions of plane stress and plane strain. The possibility to flexibly adapt the model through the use of effective moduli is particularly valuable. In the proposed framework, altering E', ν' and G' directly impacts the internal numerical moments in Eqs. (21) and (22), and consequently the governing equations.

Various combinations of constitutive models for the adherends and the adhesive were investigated to improve the analysis results. Each hypothesis is labeled as $\mathrm{H}_i^{(s)}$ or $\mathrm{H}_i^{(a)}$, where the superscript s or a refers to the substrate or the adhesive, respectively, and the subscript i denotes the hypothesis level. These hypotheses are detailed as follow:

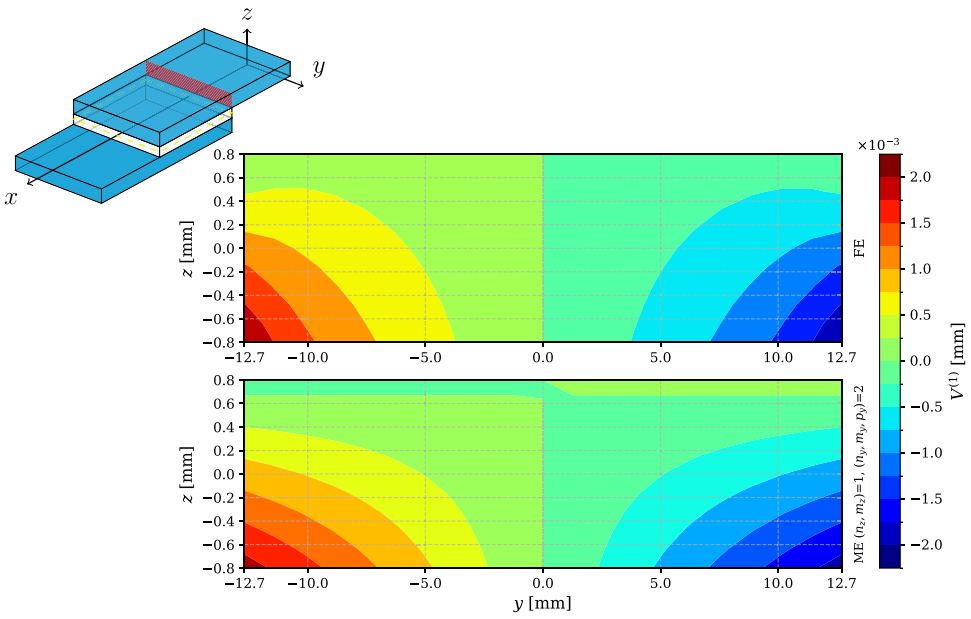

Fig. 12. Contours of FE and ME upper adherend transversal displacement on the yz plane at the beginning of the overlap region.

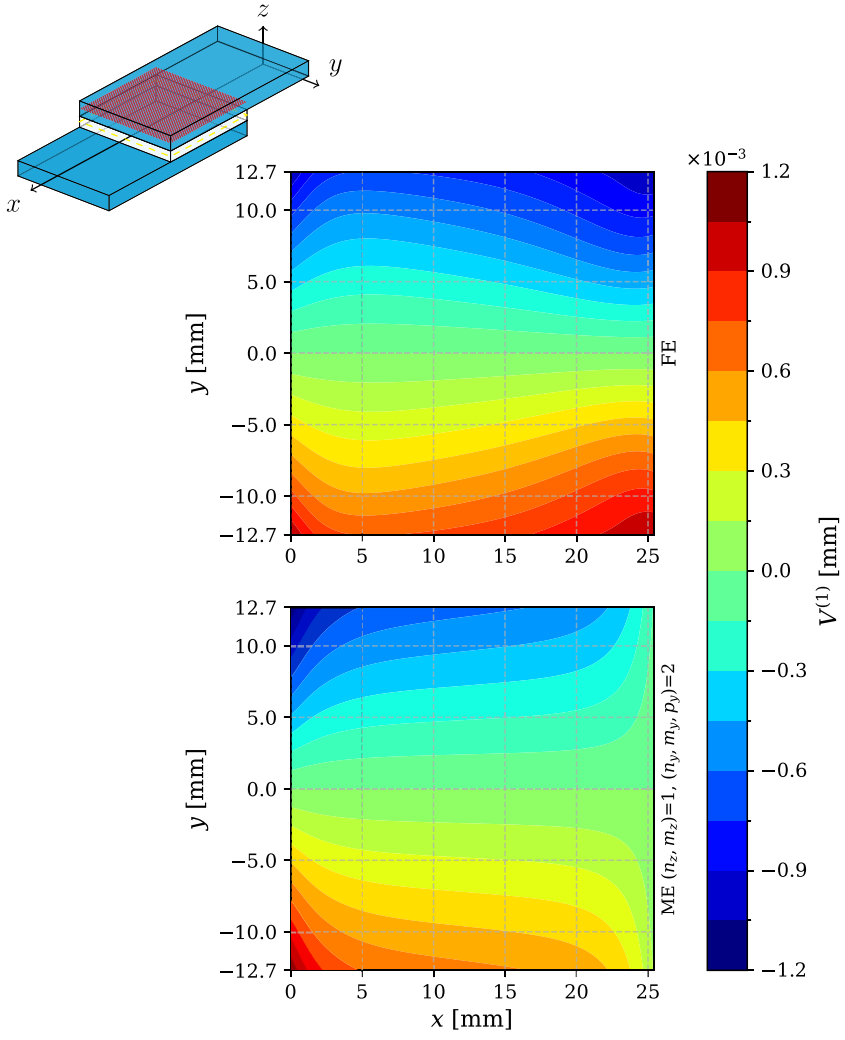

Fig. 13. Contours of FE and ME upper adherend transversal displacement on the xy plane at half-thickness in the overlap region.

Table 4
Maximum ME adhesive stresses and relative percentage difference with respect to FE for different adherend and adhesive constitutive models.

Adherend hypothesis $H_0^{(s)}$				
Adhesive hypothesis	σ_{zz} [MPa]		τ_{xz} [MPa]	
	Value	Difference [%]	Value	Difference [%]
$H_0^{(a)}$	12.7	−3.8	−8.7	−3.2
$H_1^{(a)}$	13.5	2.1	−8.7	−3.2
$H_2^{(a)}$	15.8	18.1	−8.7	−3.2
Adherend hypothesis $H_1^{(s)}$				
Adhesive hypothesis	σ_{zz} [MPa]		τ_{xz} [MPa]	
	Value	Difference [%]	Value	Difference [%]
$H_0^{(a)}$	12.0	−9.4	−8.2	−8.4
$H_1^{(a)}$	12.7	−3.8	−8.2	−8.4
$H_2^{(a)}$	14.7	11.2	−8.2	−8.4

H_0: Unmodified isotropic

$$E' = E \qquad \nu' = \nu$$

H_1: Plane stress effective

$$E' = \frac{E}{1-\nu^2} \qquad \nu' = \nu$$

H_2: 3D effective

$$E' = \frac{E\,(1-\nu)}{(1+\nu)\,(1-2\nu)} \qquad \nu' = \frac{\nu}{1-\nu}$$

and $G' = G$ across all of the above.

The effect of the adopted combination of constitutive models on the maximum stress values in the adhesive layer is reported in Table 4. Based on the previous findings, only the second-order expansion has been retained for the y-coordinate dependence of displacements, while a Reissner–Mindlin kinematic has been considered for the z-coordinate dependence. The adhesive stress τ_{yz} has not been included because of its relatively small magnitude, and the difference with respect to FE was calculated in percentage as:

$$\frac{\sigma_{ME} - \sigma_{FE}}{\sigma_{FE}} \cdot 100 \tag{29}$$

The results clearly indicate that both σ_{zz} and τ_{xy} are sensitive to the choice of adherend hypothesis, but only the former is influenced by the adhesive model. A more constrained adhesive representation leads to higher peel stress in the layer, which improves the agreement with FE when selecting $H_1^{(a)}$. In contrast, $H_2^{(a)}$ causes an overestimation of the peak values.

The $H_0^{(s)}H_1^{(a)}$ combination provides the best numerical match with the reference, with very small percentage deviations. This result is consistent with the study case of a thin adhesive layer. Moreover, it is worth mentioning that, considering the scale of the problem, even relatively higher percentage differences correspond indeed to small deviations in absolute terms (around 2 MPa).

The integration of various constitutive models demonstrates the flexibility of the proposed methodology, offering a versatile framework that can be adapted to enhance the stress analysis based on the specific behaviors of adherends and adhesives.

4. Conclusion and perspectives

In this paper, a novel extension of the ME modeling was presented. High-order polynomial expansions were used to describe the three-dimensional displacement field of bonded adherend plates. A detailed methodology was presented for deriving the governing equations of the assembly based on an elastic foundation model. The implementation within a solving algorithm was illustrated.

The proposed methodology was validated against FE results for the example case of a SLJ. Initially, classic theories were integrated in the ME for baseline verification. Subsequently, the influence of different displacement field assumptions and constitutive models was explored. The results highlighted the importance of including the presented, more advanced representations of the adherends behavior, capable of accounting for three-dimensional effects. The same holds true for the flexibility in adapting the constitutive models, especially significant in the case of the adhesive. Good agreement was shown in terms of both adhesive and adherend stress distributions.

Although the methodology improved upon previous studies that were limited to 2D representations of the substrates (Schwartz et al., 2024a), the use of an elastic foundation still represents a limitation to the accuracy of the predictions due to the inability to satisfy the zero-stress condition at the overlap ends. A more refined continuum representation of the adhesive layer, such as the one proposed in Schwartz et al. (2024b), could provide further improvements. Moreover, a more accurate characterization of the confined adhesive constitutive behavior may increase the precision of the peak values estimation.

Future works employing the ME could also address its application in dynamic analysis and damage modeling, as envisioned in Lachaud et al. (2020) and Lelias et al. (2015), thanks to its compatibility with established techniques in the field of FE involving mass matrices, in addition to stiffness matrices, and cohesive zones.

Ultimately, the methodology stands out as one of the few capable of performing approximate three-dimensional stress analysis (Banea and Silva, 2009), effectively capturing complex interactions without having to resort to FE or other mesh-based methods. In addition, the systematic selection of higher-order displacements and constitutive model provides great flexibility and accuracy.

CRediT authorship contribution statement

Marcello Calì: Writing – review & editing, Writing – original draft, Visualization, Validation, Software, Methodology, Investigation, Formal analysis, Data curation, Conceptualization. **Sébastien Schwartz:** Writing – review & editing, Supervision, Software, Resources, Project administration, Methodology, Investigation, Formal analysis, Data curation, Conceptualization. **Frédéric Lachaud:** Writing – review & editing, Supervision, Project administration. **Sofia Teixeira De Freitas:** Writing – review & editing, Supervision, Resources, Project administration, Funding acquisition. **Éric Paroissien:** Writing – review & editing, Supervision, Resources, Project administration, Funding acquisition, Formal analysis, Conceptualization.

Funding sources

This research was funded in the context of the LISA project (Lightweight Innovative Smart Aerostructures) by ANR (Agence Nationale de la Recherche), EUR TSAE and Delft University Fund Foundation.

Declaration of competing interest

The authors declare that they have no known competing financial interests or personal relationships that could have appeared to influence the work reported in this paper.

Data availability

Data will be made available on request.

References

Adams, R.D., Mallick, V., 1992. A method for the stress analysis of lap joints. J. Adhes. 38 (3–4), 199–217. http://dx.doi.org/10.1080/00218469208030455.

Adams, R.D., Peppiatt, N.A., 1973. Effect of poisson's ratio strains in adherends on stresses of an idealized lap joint. J. Strain Anal. 8 (2), 134–139. http://dx.doi.org/10.1243/03093247V082134.

Anasiewicz, K., Kuczmaszewski, J., 2021. Apparent young's modulus of the adhesive in numerical modeling of adhesive joints. Materials 14, 1–11. http://dx.doi.org/10.3390/ma14020328.

Anasiewicz, K., Kuczmaszewski, J., 2022. Apparent Young's modulus of epoxy adhesives. Materials 15, http://dx.doi.org/10.3390/ma15228060.

ASTM, 2019. D1002-10 Standard Test Method for Apparent Shear Strength of Single-Lap-Joint Adhesively Bonded Metal Specimens by Tension Loading (Metal-to-Metal). Tech. Rep., American Society for Testing and Materials, http://dx.doi.org/10.1520/D1002-10R19.

Banea, M.D., Silva, L.F.D., 2009. Adhesively bonded joints in composite materials: An overview. Proc. Inst. Mech. Eng. L 223, 1–18. http://dx.doi.org/10.1243/14644207JMDA219.

Bigwood, D., Crocombe, A., 1989. Elastic analysis and engineering design formulae for bonded joints. Int. J. Adhes. Adhes. 9 (4), 229–242. http://dx.doi.org/10.1016/0143-7496(89)90066-3.

Birro, T.V., Paroissien, E., Aufray, M., Lachaud, F., 2020. A methodology based on the coupled criterion for the assessment of adhesive-to-adherend interface crack initiation. Int. J. Adhes. Adhes. 102, http://dx.doi.org/10.1016/j.ijadhadh.2020.102664.

Budhe, S., Banea, M.D., de Barros, S., da Silva, L.F., 2017. An updated review of adhesively bonded joints in composite materials. Int. J. Adhes. Adhes. 72, 30–42. http://dx.doi.org/10.1016/j.ijadhadh.2016.10.010.

da Silva, L.F., das Neves, P.J., Adams, R., Spelt, J., 2009. Analytical models of adhesively bonded joints—Part I: Literature survey. Int. J. Adhes. Adhes. 29 (3), 319–330. http://dx.doi.org/10.1016/j.ijadhadh.2008.06.005.

Da Silva, L.F., Das Neves, P.J., Adams, R., Wang, A., Spelt, J., 2009. Analytical models of adhesively bonded joints—Part II: Comparative study. Int. J. Adhes. Adhes. 29 (3), 331–341. http://dx.doi.org/10.1016/j.ijadhadh.2008.06.007.

Ebnesajjad, S. (Ed.), 2009. Adhesives Technology Handbook, second ed. William Andrew Publishing, Norwich, NY, http://dx.doi.org/10.1016/B978-0-8155-1533-3.50004-9.

Frostig, Y., Thomsen, O.T., Mortensen, F., 1999. Analysis of adhesive-bonded joints, square-end, and spew-fillet-high-order theory approach. J. Eng. Mech. 125, 1298–1307.

Goland, M., Reissner, E., 1944. The stresses in cemented joints. J. Appl. Mech. 11, A17–A27.

Hart-Smith, L., 1973. Adhesive Bonded Single Lap Joints. NASA Technical Report CR112236, Douglas Aircraft Company, Long Beach.

He, X., 2011. A review of finite element analysis of adhesively bonded joints. Int. J. Adhes. Adhes. 31, 248–264. http://dx.doi.org/10.1016/j.ijadhadh.2011.01.006.

Lachaud, F., Paroissien, E., Michel, L., 2020. Validation of a simplified analysis for the simulation of delamination of CFRP composite laminated materials under pure mode I. Compos. Struct. 237, 111897. http://dx.doi.org/10.1016/j.compstruct.2020.111897.

Lelias, G., Paroissien, E., Lachaud, F., Morlier, J., Schwartz, S., Gavoille, C., 2015. An extended semi-analytical formulation for fast and reliable mode I/II stress analysis of adhesively bonded joints. Int. J. Solids Struct. 62, 18–38. http://dx.doi.org/10.1016/j.ijsolstr.2014.12.027.

Luo, Q., Tong, L., 2007. Fully-coupled nonlinear analysis of single lap adhesive joints. Int. J. Solids Struct. 44 (7–8), 2349–2370. http://dx.doi.org/10.1016/j.ijsolstr.2006.07.009.

Mantari, J.L., Granados, E.V., 2015. A refined FSDT for the static analysis of functionally graded sandwich plates. Thin-Walled Struct. 90, 150–158. http://dx.doi.org/10.1016/j.tws.2015.01.015.

Mortensen, F., Thomsen, O., 2002. Analysis of adhesive bonded joints: a unified approach. Compos. Sci. Technol. 62 (7–8), 1011–1031. http://dx.doi.org/10.1016/S0266-3538(02)00030-1.

Nguyen, T.H., Le Grognec, P., 2021. Analytical and numerical simplified modeling of a single-lap joint. Int. J. Adhes. Adhes. 108, 102827. http://dx.doi.org/10.1016/j.ijadhadh.2021.102827.

Ojalvo, I.U., Eidinoff, H.L., 1978. Bond thickness effects upon stresses in single-lap adhesive joints. AIAA J. 16 (3), 204–211. http://dx.doi.org/10.2514/3.60878.

Oplinger, D., 1991. A Layered Beam Theory for Single-Lap Joints. US AMTL Technical Report MTL91-23, US Army Materials Technology Laboratory.

Orsatelli, J.-B., Paroissien, E., Lachaud, F., Schwartz, S., 2024. Influence of modelling hypotheses on strength assessment of CFRP stepped repairs. Int. J. Adhes. Adhes. 132, 103682. http://dx.doi.org/10.1016/j.ijadhadh.2024.103682.

Oterkus, E., Barut, A., Madenci, E., Smeltzer, S.S., Ambur, D.R., 2004. Nonlinear analysis of bonded composite single-lap joints. In: Collection of Technical Papers - AIAA/ASME/ASCE/AHS/ASC Structures, Structural Dynamics and Materials Conference. vol. 1, American Institute of Aeronautics and Astronautics Inc., pp. 555–572. http://dx.doi.org/10.2514/6.2004-1560.

Paroissien, E., Lachaud, F., Da Silva, L.F., Seddiki, S., 2019. A comparison between macro-element and finite element solutions for the stress analysis of functionally graded single-lap joints. Compos. Struct. 215, 331–350. http://dx.doi.org/10.1016/j.compstruct.2019.02.070.

Paroissien, E., Sartor, M., Huet, J., 2007. Hybrid (bolted/bonded) joints applied to aeronautic parts: Analytical one-dimensional models of a single-lap joint. In: Tichkiewitch, S., Tollenaere, M., Ray, P. (Eds.), Advances in Integrated Design and Manufacturing in Mechanical Engineering II. Springer Netherlands, Dordrecht, pp. 95–110. http://dx.doi.org/10.1007/978-1-4020-6761-7_7.

Pizzi, A., Mittal, K., 2003. Handbook of Adhesive Technology, second ed. Taylor & Francis, http://dx.doi.org/10.1201/9780203912225.

Reddy, J.N., 1984. A refined nonlinear theory of plates with transverse shear deformation. Int. J. Solids Struct. 20, 881–896. http://dx.doi.org/10.1016/0020-7683(84)90056-8.

Schwartz, S., Paroissien, E., Lachaud, F., 2020. General formulation of macro-elements for the simulation of multi-layered bonded structures. J. Adhes. 96 (6), 602–632. http://dx.doi.org/10.1080/00218464.2019.1622420.

Schwartz, S., Paroissien, É., Lachaud, F., 2024a. An enriched finite element for the simplified stress analysis of an entire bonded overlap: Continuum macro-element. Int. J. Adhes. Adhes. 129, http://dx.doi.org/10.1016/j.ijadhadh.2023.103571.

Schwartz, S., Paroissien, É., Lachaud, F., 2024b. Extended formulation of macro-element based modelling – Application to single-lap bonded joints. Comput. Struct. 305, 107589. http://dx.doi.org/10.1016/j.compstruc.2024.107589.

Teixeira de Freitas, S., Sinke, J., 2017. Failure analysis of adhesively-bonded metal-skin-to-composite-stiffener: Effect of temperature and cyclic loading. Compos. Struct. 166, 27–37. http://dx.doi.org/10.1016/j.compstruct.2017.01.027.

Tserpes, K., Barroso-Caro, A., Carraro, P.A., Beber, V.C., Floros, I., Gamon, W., owski, M.K., Santandrea, F., Shahverdi, M., Skejić, D., Bedon, C., Rajčić, V., 2022. A review on failure theories and simulation models for adhesive joints. J. Adhes. 98, 1855–1915. http://dx.doi.org/10.1080/00218464.2021.1941903.

Volkersen, O., 1938. Die nietkraftverteilung in zugbeanspruchten nietverbindungen mit konstanten laschenquerschnitten. Luftfahrtforschung 15 (24), 41–47.

Wei, Y., Jin, X., Luo, Q., Li, Q., Sun, G., 2024. Adhesively bonded joints – A review on design, manufacturing, experiments, modeling and challenges. Compos. B 276, http://dx.doi.org/10.1016/j.compositesb.2024.111225.

Williams, J.H., 1975. Stresses in adhesive between dissimilar adherends. J. Adhes. 7 (2), 97–107. http://dx.doi.org/10.1080/00218467508075042.